Spike-frequency dependent inhibition and excitation of neural activity by high-frequency ultrasound

Martin Loynaz Prieto[1], Kamyar Firouzi[2], Butrus T. Khuri-Yakub[2], Daniel V. Madison[1], and Merritt Maduke[1]
[1]Department of Molecular and Cellular Physiology, and [2]E. L. Ginzton Laboratory, Stanford University

Condensed title: Spike-Rate-Dependent Neuromodulation by Ultrasound [50 characters or less]

SUMMARY [40 words or less] Prieto et al. describe how ultrasound can either inhibit or potentiate action potential firing in hippocampal pyramidal neurons and demonstrate that these effects can be explained by increased potassium conductance.

ABSTRACT [300 words or less]

Ultrasound can modulate action-potential firing *in vivo* and *in vitro*, but the mechanistic basis of this phenomenon is not well understood. To address this problem, we used patch-clamp recording to quantify the effects of focused, high-frequency (43 MHz) ultrasound on evoked action potential firing in CA1 pyramidal neurons in acute rodent hippocampal brain slices. We find that ultrasound can either inhibit or potentiate firing in a spike-frequency-dependent manner: at low (near-threshold) input currents and low firing frequencies, ultrasound inhibits firing, while at higher input currents and higher firing frequencies, ultrasound potentiates firing. The net result of these two competing effects is that ultrasound increases the threshold current for action potential firing, the slope of frequency-input curves, and the maximum firing frequency. In addition, ultrasound slightly hyperpolarizes the resting membrane potential, decreases action potential width, and increases the depth of the afterhyperpolarization. All of these results can be explained by the hypothesis that ultrasound activates a sustained potassium conductance. According to this hypothesis, increased outward potassium currents hyperpolarize the resting membrane potential and inhibit firing at near-threshold input currents, but potentiate firing in response to higher input currents by limiting inactivation of voltage-dependent sodium channels during the action potential. This latter effect is a consequence of faster action-potential repolarization, which limits inactivation of voltage-

dependent sodium channels, and deeper (more negative) afterhyperpolarization, which increases the rate of recovery from inactivation. Based on these results we propose that ultrasound activates thermosensitive and mechanosensitive two-pore-domain potassium (K2P) channels, through heating or mechanical effects of acoustic radiation force. Finite-element modelling of the effects of ultrasound on brain tissue suggests that the effects of ultrasound on firing frequency are caused by a small (less than 2°C) increase in temperature, with possible additional contributions from mechanical effects

INTRODUCTION

Ultrasound can non-invasively modulate action potential activity in neurons *in vivo* and *in vitro*, with improved depth penetration and spatial resolution relative to other non-invasive neuromodulation modalities, and it may therefore become an important new technology in basic and clinical neuroscience (Fry et al., 1958; Gavrilov et al., 1996; Tufail et al., 2010; Bystritsky et al., 2011; Fomenko et al., 2018; Blackmore et al., 2019). Investigation of this phenomenon has predominantly focused on low-frequency ultrasound (defined here as less than 3 MHz, although there is no firmly defined boundary between “high” and “low” frequency in the neuromodulation field), but higher ultrasound frequencies have also been shown to modulate action potential firing *in vitro* (Menz et al., 2013; Menz et al., 2019) and to directly modulate ion channel activity in heterologous systems (Kubanek et al., 2016; Prieto et al., 2018). The focus on lower frequency ultrasound is understandable, since envisioned clinical applications involving transcranial focused ultrasound have been a primary motivation for research on ultrasound neuromodulation, and loss of ultrasound power due to attenuation in the skull limits these applications to low frequency ultrasound. For applications in which transmission through the skull does not impose limits on frequency, such as *in vitro* studies, neuromodulation in the peripheral nervous system (Downs et al., 2018; Cotero et al., 2019; Zachs et al., 2019), neuromodulation using subcranial implants, or neuromodulation in experimental animal model systems involving craniotomies or acoustically transparent cranial windows, high frequencies have a distinct advantage in terms of the greater spatial resolution that can be achieved. Even for *in vivo* applications in human subjects, however, the spatial resolutions that can be achieved with low-frequency, transcranial ultrasound neuromodulation

are on the order of millimeters, making ultrasound neuromodulation superior in this respect to other, more established forms of non-invasive brain stimulation (Tyler et al., 2018).

These applications motivate investigation of the fundamental physical, cellular, and molecular mechanisms underlying neuromodulation, which are all not well understood for either high- or low-frequency ultrasound. It remains an open question to what extent these mechanisms overlap for high- and low-frequency ultrasound neuromodulation. In terms of the basic physical mechanism by which acoustic energy is transduced into effects on biological tissue, most proposed mechanisms for ultrasound neuromodulation involve either heating due to absorption of acoustic energy (Hand, 1998), mechanical effects of acoustic radiation force (Duck, 1998; Sarvazyan et al., 2010), or effects of cavitation (the nucleation, growth, oscillation, and sometimes collapse, of microscopic gas bubbles) (Leighton, 1998; Wu and Nyborg, 2008; Krasovitski et al., 2011; Plaksin et al., 2016). Of these, the first two increase with acoustic frequency, while the probability of cavitation decreases with acoustic frequency. There are also many unanswered questions at the cellular level. Both excitatory and inhibitory effects of ultrasound have been observed using direct or indirect measures of neural activity at the population level (Bystritsky et al., 2011; Blackmore et al., 2019), but it is unclear whether the direct effect of ultrasound at the cellular level is excitatory or inhibitory. Of course, the answer to this question could depend on any number of possible relevant biological and experimental variables, such as species, tissue, specific neural subtype, ultrasound stimulus parameters, or whether effects on intrinsic or evoked activity are measured. For example, a cellular-level excitatory effect, specific to GABAergic interneurons, could produce an inhibitory effect at the population level. This leads to the question of whether certain subpopulations of neurons are

more sensitive to ultrasound than others, and if so, what are the specific molecular mechanisms underlying the differences in sensitivity. Do certain ion channels respond directly to ultrasound? What biophysical properties might account for the sensitivity of these channels to ultrasound, and how might cell-type specific differences in the density and localization of these channels, and the way in which they interact with other ion channels to regulate action potential firing, produce differences in the response to ultrasound?

One reason there are so many outstanding questions regarding ultrasound neuromodulation is that patch-clamp recordings of the effects of ultrasound on action-potential firing in neurons have been unavailable. At low ultrasound frequencies, we (Prieto et al., 2018) and others (Tyler et al., 2008) have found that patch-clamp seals are extremely unstable in the presence of ultrasound at low frequencies, precluding detailed, mechanistic studies of ultrasound neuromodulation with this technique, which provides quantitative information on action-potential timing and dynamics unobtainable with other techniques. However, we have previously shown that stable patch-clamp recordings can be achieved using ultrasound at the frequency of 43 MHz (Prieto et al., 2018). Here, we use patch-clamp recording to measure the effects of ultrasound at 43 MHz and 50 W/cm^2 on action-potential firing in response to injected current in pyramidal neurons of the CA1 layer of the hippocampus in acute rodent brain slices. We find that ultrasound has a bidirectional, spike-frequency dependent effect on excitability, and that this and other observed neurophysiological effects of ultrasound can be explained by activation by ultrasound of a steady K^+ current, resembling that of two pore domain potassium channels (K2P channels).

66 **MATERIALS AND METHODS**

67 *Slice preparation.* Brain slices were prepared from male Sprague-Dawley rats, 35-50 days old.
68 Rats were anesthetized with isofluorane and decapitated, and the brain was immediately
69 removed and placed in ice-cold artificial cerebral spinal fluid (ACSF), bubbled with 95% O_2 and
70 5% CO_2. The hippocampus was dissected out and placed on the slicing apparatus, consisting of a
71 manual micrometer and a gravity-driven vertical slicing mechanism, with the CA1 layer oriented
72 approximately parallel to the slicing blade. Slices (500 microns thick) were prepared and then
73 stored in a humidified chamber with an atmosphere of 95% O_2/5% CO_2, resting on a square of
74 filter paper placed on a dish of ACSF. Slices were used within 1-6 hours of slice preparation.
75 Animals were handled in accordance with protocols approved by Stanford University's
76 Institutional Animal Care and Use Committee.

77

78 *Ultrasound.* Continuous wave ultrasound at 43 MHz and 50 W/cm^2 was applied to brain slices
79 using a set-up similar to that we previously used for our experiments on cultured cells (Prieto et
80 al., 2018), except that the tissue was visualized with a dissecting microscope at low
81 magnification. The bottom of the experimental chamber was a 25-micron film of polystyrene,
82 plasma-treated with a Harrick plasma cleaner (Harrick Plasma, Ithaca, NY). Ultrasound was
83 transmitted from below (through the polystyrene film) with the sound beam perpendicular to
84 the bottom of the chamber. The 43 MHz transducer was a custom-built device, calibrated as
85 described previously (Prieto et al., 2013), excited using an ENI 403LA (37 dB) amplifier (ENI,
86 Rochester, NY). The focal volume of the transducer is approximately a cylinder 90 microns in
87 diameter by 500 microns long, and the focal distance is approximately 4.2 mm. The set-up was

88 based on the stage from a Zeiss Axioskop-2 microscope (Zeiss Microscopes, Jena, Germany),
89 with the housing for the sub-stage condenser modified to accommodate the transducer, such
90 that the position of the transducer could be adjusted using the controls for alignment of the
91 condenser, and the position of the tissue sample relative to the transducer could be adjusted
92 with the microscope stage. The transducer was coupled to the polystyrene film at the bottom
93 of the experimental chamber using a small volume of distilled water held in place by a rubber
94 O-ring attached to the tip of the transducer with silicone grease. The focal volume of the
95 transducer was aligned along the z-axis using a pulse-echo protocol, adjusting the height of the
96 transducer to maximize the echo signal from the bottom of the empty chamber. The focus was
97 aligned in the x-y plane by adding to the chamber a small volume of ACSF, barely sufficient to
98 cover the bottom of the chamber, such that a thin layer of solution was spread over the bottom
99 of the chamber. Ultrasound pulses, one second in length, were then applied, raising a mound of
100 fluid at the focus of the transducer (due to the radiation force produced by reflection of the
101 acoustic wave at the interface between the solution and the air above it (Duck, 1998)). The
102 mound of fluid was then aligned in the x-y plane to the center of a reticle in one eyepiece of the
103 dissecting microscope, and, after adding additional ACSF and the tissue sample to the chamber,
104 the center of the reticle was aligned with the region of the tissue targeted for patch-clamp
105 recording. The ultrasound intensity (50 W/cm^2) is the spatial peak, pulse average intensity for
106 the free field. The interval between ultrasound applications was at least 12 seconds.
107
108 *Electrophysiology.* Current clamp recordings were performed using an Axon Instruments
109 Axoclamp-2B amplifier operating in “Bridge” mode and Digidata 1330A digitizer with pClamp

110 software (Molecular Devices, Sunnyvale, CA), except for the preliminary experiments in
111 Supplemental Figure 1, which were performed with an Axon Instruments Axopatch 200B
112 amplifier (Molecular Devices, Sunnyvale, CA). Patch-clamp recording was performed using a
113 "blind-patch" approach (Blanton et al., 1989; Malinow and Tsien, 1990; Castaneda-Castellanos
114 et al., 2006), in which the recording pipette was positioned above the CA1 layer of the
115 hippocampus, as identified visually at low magnification, and then slowly lowered into the
116 tissue while applying positive pressure to the pipette and monitoring the pipette tip resistance
117 in voltage-clamp mode. In the blind-patch approach, a small decrease in tip resistance is used to
118 indicate possible contact of the pipette tip with a neuron in the absence of the usual visual
119 cues. Typically, the first two instances of possible cell contact were not used, to avoid patching
120 on cells at the surface of the tissue that may have been damaged during the slicing procedure.
121 Gigaseals and the subsequent whole-cell recording configuration were obtained following the
122 standard procedure in voltage-clamp mode before switching to current-clamp mode. In most
123 experiments, slices were held in place with a Warner Instruments RC-22 slice anchor (Harvard
124 Bioscience, Hamden, CT); the experiments in Supplemental Figure 1 and some of the
125 experiments in Figure 1E were performed without a slice anchor. No obvious effects of the slice
126 anchor on the ultrasound response were noted. Series resistance, monitored and compensated
127 throughout the recording, was between 30 and 100 MΩ. All of the neurons used for
128 experiments could be unambiguously identified as pyramidal cells by their distinct adaptive
129 firing patterns in response to 2-s current steps. Current records were low-pass filtered at 10 kHz
130 and sampled at 100 kHz. Brain slices were continuously perfused with ACSF (in mM: 119 NaCl,
131 2.5 KCl, 1.3 $MgSO_4$, 2.5 $CaCl_2$, 1 NaH_2PO_4, 26.2 $NaHCO_3$, 11 glucose), bubbled with 95% O_2/5%

132 CO_2, at ~100-250 mL/hour. The internal solution was (in mM): 126 K-gluconate, 4 KCl, 10 HEPES,
133 4 Mg-ATP, 0.3 Na_2GTP, 10 Na-phosphocreatine, 10 sucrose, and 50 U/mL creatine
134 phosphokinase (porcine), pH 7.2 (KOH). This internal solution contains an ATP-regenerating
135 system (phosphocreatine and creatine phosphokinase) because we found that the strength of
136 the response to ultrasound was unstable, gradually declining over the course of a recording
137 unless the ATP-regenerating system was included (Supplemental Figure 2). Na-phosphocreatine
138 was obtained from Abcam and creatine phosphokinase was obtained from EMD Millipore. All
139 other salts and chemicals were obtained from either Sigma-Aldrich or Fisher Scientific. (For
140 some of the preliminary recordings shown in Figure 1E, the creatine phosphokinase was
141 omitted from the internal solution, or a different internal solution, containing 120 K-gluconate,
142 40 HEPES, 5 $MgCl_2$, 0.3 Na_2GTP, 2 Na_2ATP, pH 7.2 (KOH) was used. Creatine phosphokinase was
143 also omitted for the experiments in Supplemental Figure 4). Other than the reduction of the
144 ultrasound response over time in the absence of creatine phosphokinase, no obvious
145 differences in recordings with different internal solutions were noted.) Because creatine
146 phosphokinase increases the viscosity of the solution, making it difficult to obtain gigaseals, a
147 small volume of internal solution without the enzyme was added to the tip of the pipette
148 (enough to fill approximately the first 3 mm of the tip) before back-filling the pipette with the
149 enzyme-containing solution. Pipettes were pulled from thick walled glass and had resistances
150 between 5 and 10 MΩ. Recordings were performed at room temperature (21-23°C), except for
151 the experiments in Supplemental Figure 4, which were performed at near physiological
152 temperature (30°C). For these experiments, the temperature of the external solution was
153 regulated and monitored with a Warner Instruments CL-100 bipolar temperature controller

154 equipped with a SC-20 in-line heater/cooler and a thermistor (Warner Instruments, Hamden,
155 CT). The external solution was heated to 35-37°C while being bubbled with 95% O_2/5% CO_2 and
156 then passed through the heater/cooler and cooled to achieve the target temperature of 30°C in
157 the bath solution. (The external solution was cooled rather than heated to avoid loss of oxygen
158 tension and formation of gas bubbles due to heating of oxygen-saturated solution.)
159
160 *Data analysis.* Current records were analyzed in Igor Pro (Wavemetrics, Lake Oswego, OR) with
161 user-written procedures. Action-potential threshold was defined as the point at which the first
162 derivative of the voltage reached 4% of its peak value during the rising phase of the action
163 potential. This quantitative criterion was previously found to correspond with action-potential
164 thresholds as identified visually (Khaliq and Bean, 2010; Yamada-Hanff and Bean, 2015), and we
165 found that it also works well with our data, using phase plots to visually confirm the threshold
166 value. Action-potential height was defined as the difference between the action-potential peak
167 and the action-potential threshold voltage. Action-potential width was measured at 50% of
168 action potential height defined in this manner. Threshold current levels for action-potential
169 firing were estimated based on a series of current steps in 10-pA increments. Frequency-input
170 plots and action-potential parameters (height, width, latency, and interspike intervals) were
171 determined from the average values of at least 3 trials each for the control and ultrasound
172 conditions. Frequency-input trials were performed alternatingly for the control and ultrasound
173 conditions, with the first condition tested varying randomly on a cell-by-cell basis.
174 Average traces for analysis of the effects of ultrasound on membrane resting potential and
175 membrane capacitance were derived from at least 3 voltage traces.

176 Statistical significance was assessed using paired or unpaired two-tailed Student's t-tests, with P
177 < 0.05 defined as significant. Statistical analysis was performed in Microsoft Excel.
178
179 *Finite-element simulations.* Finite-element were performed in COMSOL (COMSOL Inc., Palo
180 Alto, CA, USA). The simulation domain had radially symmetric geometry and was 6 mm in the
181 axial direction. The simulation domain contained four layers of different materials: a lower layer
182 of water (4.2 mm thick in the axial direction), followed by a layer of polystyrene (25 microns
183 thick), followed by a layer of brain tissue (500 microns thick), followed by an upper layer of
184 water (1.275 mm thick). The width of the simulation domain in the axial direction was 1 mm
185 (for simulation for acoustic pressure and heating) or 5 mm (for simulation of mechanical
186 deformation) in the axial direction. A 940-micron diameter by 100-micron height arc on the
187 lower axial boundary of the simulation domain represented the quartz lens of the transducer.
188 Simulations of acoustic pressure, heating, and static displacement in response to
189 radiaton force were performed as described previously (Prieto et al., 2018). For simulation of
190 dynamic tissue displacement in response to radiation force, the brain slice was modeled as a
191 incompressible, linear viscoelastic material (Calhoun et al., 2019), characterized by Young's
192 modulus, Poisson's ratio, and shear viscosity, loaded by the fluid layer above it. The polystyrene
193 was modeled as a linear elastic material, because we determined in a series of simulations that
194 including viscosity of the polystyrene had no effect on the tissue displacement. A time step of
195 0.1 ms was used for simulation of the dynamic tissue displacement. Material properties used
196 for water, polystyrene, and brain tissue used in the simulation and sources for these values are

given in Table 1. Additional details on mesh size, boundary conditions, and solver configurations are available in Prieto et al. (2018).

SUMMARY OF SUPPLEMENTAL MATERIAL

Supplemental materials include four figures showing: the effect of ultrasound at different intensities on action potential firing frequency (Supplemental Figure 1); stabilization of the response to ultrasound by an ATP-regenerating system in the internal solution (Supplemental Figure 2); effect of ultrasound on action potential height (Supplemental Figure 3); and the effects of ultrasound on action potential firing and waveform at near physiological temperature (30°C) (Supplemental Figure 4).

RESULTS

We measured the effects of ultrasound on action-potential firing in hippocampal CA1 pyramidal cells using the set-up shown in Figure 1A (described in *Materials and Methods*). Throughout the experiments reported here, ultrasound was applied at 43 MHz and 50 W/cm^2 as a 1-s, continuous-wave pulse. In an initial exploration of the effects of intensity on the ultrasound response, we determined that 50 W/cm^2 had a sufficiently robust effect on firing frequency to permit quantitative investigation of this effect (Supplemental Figure 1), but we did not perform a detailed investigation of the intensity dependence. We chose to use continuous-wave ultrasound (without additional low-frequency modulation within the pulse) because continuous-wave ultrasound was previously found to be optimal for ultrasound neuromodulation of retinal ganglion cells at 43 MHz (Menz et al., 2013). With these ultrasound

219 parameters, we found robust, reproducible inhibition of action-potential firing by ultrasound
220 using the protocol illustrated in Figure 1B. In these experiments, a current-injection amplitude
221 sufficient to induce firing at an average frequency of ~4-12 Hz during the first 500 ms of the
222 current step (corresponding to the overlap between the ultrasound stimulus and current step)
223 was used. This range of firing frequencies is physiologically relevant and sufficient to detect
224 either inhibition or potentiation of firing. With these experimental conditions, we established
225 that the response to ultrasound is highly reproducible, both on a trial-by-trial basis within the
226 same cell (Figure 1C-D), and between cells, with similar effects seen in over fifty cells (Figure
227 1E). In addition, the response to ultrasound was stable over the course of recordings lasting
228 over 30 minutes (Figure 1F, Supplemental Figure 2); in a few cases where the patch seal lasted
229 for over 90 minutes, the ultrasound response remained stable.
230
231 *Effects of ultrasound on frequency-input curves.* To explore the effects of ultrasound on
232 excitability over a wider range of firing frequencies, we generated frequency-input (f-i) curves
233 comparing average firing frequencies as a function of input current in the presence and
234 absence of ultrasound. An example f-i curve generated with the protocol illustrated in Figure 1B
235 is shown in Figure 2A, along with example voltage traces in Figure 2B. The average spike
236 frequency during the first 500 ms of the current step was compared to the spike frequency in
237 the same time window in the absence of ultrasound. To compare the effects of ultrasound
238 across neurons, we converted the f-i curves into plots of the relative increase or decrease in
239 firing frequency as a function of the input current (Figure 2C-D). These data reveal two distinct
240 regimes with contrasting inhibitory and excitatory ultrasound effects. At relatively low input

241 currents, near the threshold for action-potential firing under this current stimulation protocol,
242 ultrasound decreases the average firing frequency; while at relatively high input currents, well
243 above the action-potential threshold, ultrasound increases the average firing frequency.
244 Between these two regimes, there is a transitional region where there is little or no effect on
245 average firing frequency, presumably due to the balance between competing inhibitory and
246 excitatory effects. Other notable effects of ultrasound on the f-i curves are an increase in the
247 threshold current for action-potential firing, an increase in the slope of the f-i relationship in
248 the approximately linear region of the f-i curve, and an increase in the maximum firing
249 frequency in the sublinear "plateau" region of the curve (Figure 2A). The mean (± SEM) slope of
250 linear region of the f-i curve increased from 0.108 ± 0.007 Hz/pA in the control condition to
251 0.145 ± 0.012 Hz/pA in the ultrasound condition; and the mean maximum firing frequency
252 increased from 23 ± 1 Hz in the control condition to 30 ± 2 Hz/pA in the ultrasound condition (N
253 = 9).
254 Action-potential firing behavior is determined by the interaction between numerous K^+,
255 Na^+, and other ionic currents (Madison and Nicoll, 1984; Bean, 2007). Some of these currents
256 are clearly identified with specific ion channel subtypes, while the molecular identity of others
257 is still uncertain. Thus, f-i curves are a complicated function of the density, localization,
258 conductance, and kinetic properties of these channels/currents. Some currents inactivate
259 relatively rapidly and only influence firing frequency during the initial response to a sustained
260 depolarizing current step, while others show slow, voltage-dependent activation, and only
261 influence firing frequency late in a current step; still other currents can influence firing
262 frequency throughout a sustained depolarization. To explore the molecular basis of the

263 response to ultrasound, we therefore generated a second set of f-i curves with ultrasound
264 applied 1 s after the start of a 3-s current step (Figure 3A).
265 Ultrasound also had a bidirectional, spike-frequency-dependent effect on excitability
266 when it was applied 1 second after the start of a current step (Figure 3). Again, ultrasound
267 decreased firing frequency in the low-firing-frequency, near-threshold region of the f-i curve,
268 and increased spike rate in the high-firing-frequency, suprathreshold region of the curve (Figure
269 3B-D). However, the excitatory effect was more pronounced than we observed when the
270 ultrasound pulse started 500 ms before the start of the current step. Here, ultrasound
271 potentiated firing frequency by several hundred percent for high input currents (Figure 3D), as
272 compared with a maximum potentiation of 49 ± 16% at 450 pA seen with the earlier ultrasound
273 application (Figure 2C). This reflects the fact that in response to prolonged injection of high
274 amplitude currents, accumulation of voltage-gated Na^+ channel (Na_V channel) inactivation can
275 drive pyramidal cells into a refractory state where spiking is infrequent and irregular or entirely
276 absent (for example, the voltage trace for the control condition at +450 pA in Figure 3C shows
277 an initial steep decline in action potential height, followed by a gradual partial recovery of
278 action potential height, followed by a period of no action potential activity). If neurons are in
279 this refractory state during the ultrasound application, ultrasound can "rescue" firing (as in the
280 example voltage trace for the ultrasound condition at +450 pA in Figure 3C). This refractory
281 state probably does not occur under normal physiological conditions, but the ability of
282 ultrasound to rescue action-potential firing under these conditions still provides an important
283 clue as to the molecular mechanisms underlying the effects of ultrasound on firing frequency,
284 as discussed further below. A hint of this rescue phenomenon is also seen when the ultrasound

285 application starts before the current step, as seen in the abrupt increase in the potentiation
286 effect at +450 pA (Figure 2C).
287
288 *Effects of ultrasound on interspike intervals.* To examine the effects of ultrasound on action-
289 potential firing in more detail we compared the latency to the first spike, and the intervals
290 between subsequent spikes (interspike intervals), in the control and ultrasound conditions
291 (Figure 4). To summarize these results, and to account for the variability in intrinsic excitability
292 between cells, we averaged *instantaneous* firing frequencies (latency and interspike intervals)
293 across cells firing at approximately the same *average* firing frequency (either 5, 10, or 20 Hz) in
294 the control condition at whatever input current was necessary to achieve these average firing
295 frequencies, and at the same input current in the ultrasound condition (Figure 4A-C). We note,
296 however, that this averaging procedure can obscure some of the details of ultrasound's effects.
297 At 5 Hz the effect of ultrasound applied 500 ms before the start of the current step is
298 predominantly inhibitory (as seen in the longer average latency and interspike intervals in the
299 ultrasound as compared with the control condition (Figure 4A), but the interval between the
300 first and second spikes was actually shorter in the ultrasound condition than the control
301 condition in some cells (6 out of 13 cells in this data set). This effect occurs because, even at
302 relatively low average firing frequencies, pyramidal cells will occasionally fire "doublets" or
303 high-frequency bursts of two action potentials, in which a second action potential is triggered
304 by the after-depolarization of the initial action potential. When this occurs, ultrasound
305 decreases the interval between spikes (Figure 4D). This result indicates that the mechanism by
306 which ultrasound potentiates firing at high average firing frequencies is also active under

307 conditions of low overall average firing frequency, during localized periods of high-frequency
308 firing. A similar combination of inhibitory and excitatory effects can be observed at 10 Hz and
309 even 20 Hz (Figure 4B-C). At 20 Hz, ultrasound still increased the latency to the first spike (16 ±
310 2 ms versus 12 ± 1 ms in the control condition; N = 12, P = 5.2 x 10^{-4}, paired, two-tailed
311 Student's t-test), despite decreasing the interspike interval for all subsequent spikes (Figure 4C).
312 The effect of ultrasound was also mixed when ultrasound was applied 1 s after the start of the
313 current step (Figure 4E).
314
315 *Effects of ultrasound on resting membrane potential.* Ultrasound also has effects on resting
316 membrane potential, which can be observed by averaging several voltage traces aligned to the
317 onset of the ultrasound pulse, in the absence of injected current. As shown in Figure 5A,
318 ultrasound has a slight hyperpolarizing effect on resting membrane potential. The average
319 voltage traces also show another interesting effect of ultrasound. In addition to the relatively
320 constant hyperpolarization, there is a transient *depolarization* of the resting membrane
321 potential, preceding the hyperpolarization effect and acting on a faster time scale, at the onset
322 of the ultrasound pulse; this transient depolarization is matched by a roughly symmetrical
323 transient hyperpolarization at the offset of the pulse (Figure 5A, *arrows*). The symmetrical,
324 on/off nature of these transients suggests that they are caused by changes in membrane
325 capacitance, as does the fact that they occur much faster than the steady-state changes in
326 resting membrane potential (Figure 5A-C). (Changes in membrane potential due to changes in
327 capacitance can occur much faster than those due to ionic currents because they do not involve
328 actual redistribution of charges across the membrane and are therefore not limited by

329 membrane conductance). Thus, the results in Figure 5 can be described by three distinct steps:
330 1) ultrasound rapidly increases membrane capacitance (C) at the onset of the ultrasound pulse,
331 which causes the membrane voltage (V) to become less negative (due to an increase in the
332 denominator in the equation V=Q/C, where Q is the negative total charge on the membrane);
333 2) ionic currents then slowly change the membrane voltage to a steady-state value determined
334 by the total ionic current (one or more ion channels having been affected by ultrasound)
335 resulting in membrane hyperpolarization; 3) at the offset of the ultrasound pulse, capacitance
336 rapidly relaxes back to its initial value, producing a transient decrease in membrane voltage,
337 through essentially the same mechanism as in step 1. We investigate the physical basis of these
338 capacitance changes and their relationship to the effects of ultrasound on excitability further
339 below, but one point worth mentioning here is that the change in capacitance is too small for
340 its effect on the rate of membrane charging (less than 1% change in membrane time constant)
341 to have a significant effect on excitability in and of itself.
342
343 *The K2P channel hypothesis.* What ion channels might be responsible for the effects of
344 ultrasound on excitability and resting membrane potential? A compelling hypothesis—able to
345 explain all of our data—is that ultrasound activates a fast-activating, non-inactivating potassium
346 channel, such as members of the K2P potassium channel family. While commonly described as
347 "voltage-independent", K2P channels (with the exception of TWIK-1 channels) actually have an
348 outwardly-rectifying, voltage-dependent open probability under physiological K^+ gradients due
349 to the interaction of permeant ions in the selectivity filter with an activation gate (Schewe et
350 al., 2016). Nonetheless, their rate of activation is fast (millisecond time-scale) and voltage-

351 independent, such that they are functionally similar to truly voltage-independent channels with
352 outwardly rectifying single-channel conductance. A primary reason for suspecting K2P channels
353 is that the effects of ultrasound are similar regardless of whether ultrasound is presented 500
354 ms before or 1 s after the start of the current step (compare Figures 2 and 3), consistent with
355 the idea that ultrasound affects a channel that does not undergo prolonged voltage-dependent
356 inactivation during sustained depolarizations. Related to this point, the effects of ultrasound
357 are not diminished by repetitive, high-frequency action potential firing (for example, in Figure
358 4C effects of ultrasound are clearly present throughout the entire 20-Hz, 10-spike train).
359 Further, a striking feature of the effects of ultrasound on spike intervals is that ultrasound
360 always increases the latency to the first spike (Figure 4A-C), regardless of the input current and
361 the rate of approach to the initial action potential threshold, consistent with the idea that
362 ultrasound affects a fast-activating, non-inactivating channel.
363 CA1 pyramidal neurons express a variety of K2P channel subunits. Expression of TASK-1
364 and TASK-3, TREK-1 and TREK-2, TRAAK, and TWIK has been shown at the mRNA level (Talley et
365 al., 2001), while expression at the protein level has been shown has been shown for TASK-3 in
366 CA1 pyramidal neurons specifically (Marinc et al., 2014), and for TRAAK throughout the central
367 nervous system (Brohawn et al., 2019). In addition, functional expression of TASK-like currents
368 has been shown in CA1 pyramidal neurons using patch-clamp recording (Taverna et al., 2005).
369 TREK and TRAAK channels are particularly interesting in the present context since they are
370 exceptionally sensitive to mechanical force and to increases in temperature between
371 approximately 20 and 40°C (Maingret et al., 2000; Kang et al., 2005). Thus, TREK and TRAAK

372 channels are responsive to the two leading candidate mechanisms by which ultrasound at 43
373 MHz could modulate ion channel activity.
374 Activation of K2P channels by ultrasound could account for all of the neurophysiological
375 effects of ultrasound described so far: hyperpolarization of resting membrane potential;
376 inhibition of action-potential firing in response to near-threshold current injections; and—
377 although this last point may seem counter-intuitive—potentiation of action potential firing at
378 high firing frequencies. Hyperpolarization of resting membrane potential by increased outward
379 K^+ current is straightforward, as is the idea that K^+ current can inhibit firing, but K^+ current can
380 also potentiate firing by its effects on action-potential repolarization and afterhyperpolarization
381 (AHP). By accelerating the rate of membrane repolarization following the peak of an action
382 potential (thereby reducing action potential width) K^+ current can reduce inactivation of
383 voltage-dependent Na^+ channels during the action potential, and by increasing the depth of the
384 AHP, it can accelerate the voltage-dependent recovery of Na_V channels from inactivation. Both
385 of these effects would tend to increase the population of Na_V channels available for activation
386 in response to depolarizing current and would increase the maximum action potential firing
387 frequency, as we in fact see in response to ultrasound (Figures 2 and 3). This mechanism is well-
388 known and widespread in neurophysiology, with several K^+ channels, including both K2P
389 channels and voltage-dependent K^+ channels (K_V channels), having been shown to facilitate
390 high-frequency firing (Lien and Jonas, 2003; Brickley et al., 2007; Gu et al., 2007; Gonzalez et al.,
391 2009; Liu and Bean, 2014; Kanda et al., 2019). The idea that the potentiation of firing by
392 ultrasound is due to effects on action-potential repolarization and AHP is supported by the
393 results in Figure 4C. For neurons firing at an average firing frequency of 20 Hz in the absence of

394 ultrasound, ultrasound increases the latency to the first spike, while it decreases the intervals
395 between all subsequent spikes. The lack of a potentiating effect on the first spike, despite the
396 otherwise strongly potentiating effects of ultrasound, indicates that the potentiating effect acts
397 through a process (such as action-potential repolarization and AHP) that occurs *after* the
398 initiation of the first action potential. The idea that ultrasound can potentiate firing by
399 activating K^+ current makes specific predictions about the effects of ultrasound on action
400 potential waveform: ultrasound should accelerate repolarization, decrease action potential
401 width, and increase the depth of the AHP.
402
403 *Effects of ultrasound on action-potential waveform.* To test the idea that potentiation of firing
404 by ultrasound is due to activation of K^+ channels, we examined the effects of ultrasound on
405 action-potential waveform in our recordings. The effects of ultrasound on action-potential
406 waveform are consistent with the idea that ultrasound facilitates high-frequency firing by
407 accelerating action-potential repolarization. Figure 6A-F shows the effect of ultrasound applied
408 500 ms before the start of the current step on action-potential width for cells firing at average
409 frequencies of 5, 10, and 20 Hz. (Ultrasound also had effects on action-potential height,
410 although these were less pronounced than the effects on width; effects on height are detailed
411 in Supplemental Figure 3.) Ultrasound decreased action-potential width for every action
412 potential at all firing frequencies. As shown in Figure 6G-H, ultrasound also decreased action-
413 potential width when applied 1 s after the start of a current step, again indicating that the
414 channels responsible for these effects continue to influence firing frequency and remain
415 responsive to ultrasound throughout sustained depolarizing current steps.

416 The effects of ultrasound on action-potential width tended to counteract the
417 broadening of action-potential width that occurs during high-frequency firing. Figure 7 plots
418 action potential width as a function of action potential number and input current for the
419 control and ultrasound conditions. In the control condition, there are dramatic differences in
420 width between the first action potential and subsequent action potentials at high input
421 currents, while in the ultrasound condition these differences are much less pronounced. To
422 quantify this effect, we measured the difference in width between the first and third, first and
423 fifth, and first and last action potentials during the ultrasound stimulus, in response to a +450
424 pA current step for the control and ultrasound conditions. These differences (mean ± SEM,
425 control vs. ultrasound, N = 9) were 2.6 ± 0.9 vs. 0.7 ± 0.1 ms, 1.5 ± 0.1 vs. 0.5 ± 0.1 ms, and 1.2 ±
426 0.2 vs 0.5 ± 0.1 ms for the third, fifth, and last action potentials (P = 0.064, 1.4×10^{-5}, and
427 0.0013, paired, two-tailed Student's t-test). One plausible interpretation of this result is that
428 K2P channels activated by ultrasound cause the membrane voltage during the action potential
429 to repolarize before slower-activating K_V channels, which would otherwise contribute to action-
430 potential repolarization, are activated. Since time-dependent activation and inactivation of K_V
431 channels causes action-potential broadening during repetitive firing (Giese et al., 1998; Shao et
432 al., 1999; Yue and Yaari, 2004; Kim et al., 2005; Gu et al., 2007), an increase in the contribution
433 of K2P channels lacking time-dependent inactivation with a concomitant decrease in the
434 contribution of K_V channels to action-potential repolarization would reduce time- and
435 frequency-dependent action potential broadening.
436 Although the effects of ultrasound on action-potential widths are predominantly due to
437 acceleration of the repolarization phase, we also noted effects on the rising phase of the action

438 potential. These effects are readily apparent in the first derivative of membrane voltage during
439 the action potential (Figure 8A) or in action potential phase plots (plots of the first derivative of
440 voltage versus voltage, Figure 8B). In fact, the maximum rates of voltage rise and fall during the
441 action potential were both consistently increased by ultrasound throughout a spike train
442 (Figure 8C-D). The effect on the falling phase is to be expected based on the observed decrease
443 in spike width and the hypothesis that ultrasound activates K2P channels. The effect on the
444 rising phase is also consistent with this hypothesis, as activation of K2P leading to reduced Na_V
445 channel inactivation would increase the number of Na_V channels available to activate during
446 the rising phase of the action potential. Alternatively, increased K2P conductance could
447 increase the rate of action potential rise by decreasing the membrane time constant (Brickley et
448 al., 2007). Consistent with these results, decreases in the rates of action-potential rise and fall
449 were seen with knock-outs of K2P channels in cerebellar granule neurons (Brickley et al., 2007)
450 and hypothalamic hypocretin/orestin neurons (Gonzalez et al., 2009), while in a heterologous
451 action-potential firing model higher levels of K2P expression increased the rate of action-
452 potential rise (MacKenzie et al., 2015).
453 In addition to effects of ultrasound on the rising and falling phases of the action
454 potential, we also found effects on the AHP. To quantify these effects, we measured the voltage
455 minimum between action potentials during repetitive firing. Because measurements of this
456 parameter are very sensitive to changes in resting membrane voltage and series resistance that
457 can occur over long recording times, we compared voltage minimums before, during, and after
458 ultrasound application within the same voltage trace (Figure 9A-B) and made a similar
459 comparison for control recordings. We performed these comparisons for ultrasound applied 1 s

460 after the start of a current, for cells firing at an average frequency of 5 Hz in the control
461 condition. This firing frequency is near the transition region between the inhibitory and
462 potentiating effects of ultrasound on spike frequency, such that the spike frequency is similar
463 for the control and ultrasound conditions, allowing us to compare a similar number of
464 interspike voltage minima for the control and ultrasound conditions (Figure 9C). This analysis
465 demonstrates that the depth of the AHP is greater during the ultrasound application than
466 before or after it, or during the same time windows for the control condition. Together with the
467 effects of ultrasound on spike waveform (Figure 6), this result supports the idea that ultrasound
468 activates a sustained outward current, which limits Na_V channel inactivation and thereby
469 potentiates high-frequency firing. Removal of Na_V channel inactivation by membrane
470 hyperpolarization also explains how ultrasound can rescue spiking in neurons that have entered
471 a refractory state due to accumulation of Na_V channel inactivation (Figure 3C, *bottom right*).
472
473 *Physical mechanism of neuromodulation by high-frequency ultrasound.* The idea that
474 ultrasound acts on K2P channels is also consistent with the physical effects of ultrasound on
475 biological tissue. At 43 MHz, two plausible mechanisms through which ultrasound might
476 modulate the activity of ion channels are heating and mechanical stress due to acoustic
477 radiation force. Absorption of acoustic energy by biological tissue as heat can increase its
478 temperature, with effects on ion channel gating and all other biological reactions. Absorption
479 also results in attenuation of ultrasound intensity as the wave propagates, creating spatial
480 gradients in intensity that give rise to radiation force, which in turn produces tissue
481 displacement and strain. At the microscopic scale, this displacement and strain may involve

482 increased tension in the cell membrane, cytoskeleton, and extracellular matrix, all of which may
483 affect excitability through mechanical effects on ion channel proteins. Among the K2P channels
484 that may be expressed by CA1 pyramidal cells, TREK and TRAAK channels are especially
485 sensitive to thermal and mechanical stimuli.

486 To gain further insight into these physical mechanisms, we performed finite-element
487 simulations of the effects of ultrasound on brain slices in the context of our experimental set-
488 up. The simulated spatial profiles of ultrasound-induced heating and macroscopic tissue
489 displacement in response to radiation force are shown in Figure 10A-B. Notably, the spatial
490 profiles of heating and displacement effects are significantly wider than the 90-micron diameter
491 of the focal volume of the ultrasound beam, with significant heating and displacement
492 occurring several hundreds of microns away from the beam axis (Figure 10C). This is an
493 important result because the thermo- and mechanosensitive K2P channels TREK-1 and TRAAK
494 are expressed at high density at the nodes of Ranvier of vertebrate neurons (Brohawn et al.,
495 2019; Kanda et al., 2019). The first node of Ranvier is located approximately 100 microns from
496 the axon initial segment (Kole, 2011). In our experiments, the soma of the patched neuron is
497 located approximately on the axis of the ultrasound beam (see *Materials and Methods*) so the
498 first node of Ranvier is probably within the region of the tissue exposed to thermal and
499 mechanical effects of ultrasound. Axonal K^+ channels play important roles in regulating
500 excitability (Shah et al., 2008; Kole, 2011; Kanda et al., 2019). It is therefore plausible that a
501 subpopulation of TREK-1 or TRAAK channels at the nodes of Ranvier could contribute to the
502 neurophysiological effects of ultrasound. The magnitude of the temperature change is also
503 consistent with a thermal mechanism for the effects of ultrasound. The maximum temperature

504 change in the simulation is 1.3 C; temperature changes of this size have previously been shown
505 to affect neural excitability (Owen et al., 2019). The maximum value of the simulated
506 displacement (1.7 microns) is similar to the displacement measured in the retina during
507 ultrasound neuromodulation with stimulus parameters similar to those used here (Menz et al.,
508 2019).

509 Since the activity of TREK and TRAAK channels is highly temperature-sensitive, we
510 considered whether our results might represent an artefact due to the experiments being
511 performed at room temperature (21-23°C). Room temperature is near the threshold for
512 temperature activation of these channels, such that they are mainly inactive in the absence of
513 other stimuli such as membrane tension, lipid agonists, or acidic pH (Maingret et al., 2000; Kang
514 et al., 2005). Thus at room temperature in the absence of additional gating stimuli, the relative
515 increase in thermosensitive K2P current would be greater in our experiments than at
516 physiological temperatures, which might lead us to overestimate the importance of K2P
517 channels in the response to ultrasound. On the other hand, the midpoints of the temperature-
518 activation curves for TREK and TRAAK channels are near 37°C (in other words, near body
519 temperature in mammals) so that the absolute increase in K2P current in response to increased
520 temperature is near maximal at physiological temperatures, so we might instead be
521 underestimating the thermal effects of ultrasound on K2P channels that would occur in
522 physiological contexts. To cut through this speculation and address these issues, we repeated
523 our experiments measuring the neurophysiological effects of ultrasound in cells firing at a spike
524 frequency of approximately 5 Hz at near-physiological temperature (30°C) (Supplemental Figure
525 4). Similar to what we observed at room temperature, ultrasound inhibited action potential

526 firing at this relatively low spike frequency and decreased action potential width, indicating that
527 these effects are not especially sensitive to the ambient temperature. However, the
528 hyperpolarizing effect of ultrasound on the resting membrane voltage that we observed at
529 room temperature was no longer apparent at 30°C, possibly due to increased noise in the
530 baseline voltage or more hyperpolarized (in other words, closer to the K^+ reversal potential)
531 resting voltage at higher temperature.

532 It is instructive to consider the amplitude and time course of the membrane capacitance
533 change in response to ultrasound (Figure 5) in the context of possible thermal and mechanical
534 mechanisms. As described above (under *Effects of ultrasound on resting membrane potential*),
535 the capacitance change in response to ultrasound is fast relative to the membrane time
536 constant, so we can assume that the total charge on the membrane is constant during the
537 initial transient depolarization in response to ultrasound (Figure 5A, *left arrow*). In other words,
538 the numerator in the equation $V = Q/C$ is constant, so for small changes in voltage the relative
539 change in voltage is approximately inversely proportional to the relative change in capacitance.
540 Empirically, membrane capacitance increases by approximately 1% per degree C (Taylor, 1965).
541 This is consistent with the size of the simulated temperature rise (peak simulated temperature
542 rise of 1.3°C compared with the measured amplitude of the initial decrease in voltage of 0.7 ±
543 0.1%). However, the time course of the temperature rise (Figure 10D) is much slower than the
544 time course of the voltage transient (which again, assuming constant Q, is identical to the time
545 course of the capacitance change). The time course of the change in resting membrane
546 potential (173 ± 18 ms, Figure 5), however, parallels that of the temperature rise. (A
547 capacitance change on the time course of the simulated temperature rise would not have a

548 significant effect on the membrane voltage, as it would be counteracted by ionic currents.)
549 Thus, the simulated ultrasound heating results strongly suggest that ultrasound affects action-
550 potential firing in our experiments at least in part through a thermal effect on ion channels, but
551 do not explain the presence of the capacitive transients.

552 We considered whether the time course of the capacitive transients could instead be
553 explained by the dynamics of the tissue mechanical response to acoustic radiation force. We
554 sought to determine whether, having already modeled the static displacement of the tissue, we
555 could, without retroactively changing any of the tissue material properties, obtain a time course
556 for tissue displacement similar to that of the capacitive transients using a simple viscoelastic
557 model with reasonable tissue viscous properties (see *Materials and Methods*). We found that
558 this could be achieved using a shear viscosity (μ) of 1 Pa·s (Figure 10E). Since the tissue is
559 essentially incompressible in our model (Poisson's ratio (ν) = 0.4998), this is equivalent to a
560 relaxation time of $2\mu\cdot(1+\nu)/E$ = 6 ms (where E is Young's modulus). Biological tissue is a highly
561 heterogeneous material that displays a variety of active and passive mechanical responses to
562 force, spanning time scales from milliseconds to hours (Ricca et al., 2013), and as a result its
563 viscous properties are highly sensitive to the time scale of the measurement and even complex
564 viscoelastic models encompassing multiple relaxation times may not fully describe the
565 viscoelastic behavior of tissue. Nonetheless, the shear viscosity/relaxation time in our model is
566 reasonable for a soft, gel-like material, and is comparable to fast relaxation times observed
567 experimentally in brain tissue (Arbogast and Margulies, 1999; Abolfathi et al., 2009; Rashid et
568 al., 2012, 2013). Moreover, the simulated time course of displacement is consistent with
569 experimental measurements of the tissue displacement in response to ultrasound at 43 MHz

570 and 40 W/cm^2 in the salamander retina, which was found to be complete in less than 10 ms
571 (Menz et al., 2019).
572 We can therefore make the reasonable assumption that the capacitive transients are
573 due to a mechanical effect on membrane properties, and we can estimate the size of the
574 potential ion-channel gating effects that would occur as a result of this mechanical effect. The
575 capacitance of a lipid bilayer membrane is given by $C = \varepsilon \cdot \varepsilon_0 \cdot A/L$, where ε is the dielectric
576 constant of the hydrophobic core of the lipid bilayer, ε_0 is the permittivity (polarizability) of free
577 space, A is membrane area, and L is the thickness of the hydrophobic core of the membrane.
578 For small strains like those under consideration here, lipid bilayer membranes can be
579 considered incompressible, such that a 1% increase in capacitance corresponds to a 0.5%
580 increase in area and a 0.5% decrease in thickness (White and Thompson, 1973; Alvarez and
581 Latorre, 1978). An increase in membrane area can be converted to an increase in membrane
582 tension (γ) according to $\gamma = \Delta A \cdot K_A$, where ΔA is the relative change in area and K_A is the area
583 elastic constant of the membrane. Area elastic constants measured for lipid membranes are on
584 the order of 100's of mN/m (Evans et al., 1976; Kwok and Evans, 1981; Needham and Nunn,
585 1990). If the capacitance transients are due to membrane strain, the resulting membrane
586 tension is on the order of a few 0.1 mN/n to a few mN/m. These values are similar to the
587 tension thresholds for activation of mechanosensitive K2P channels (estimated as 0.5-4 mN/m
588 for activation of TREK-1 and TRAAK (Brohawn et al., 2014)), which are low relative to other
589 known mammalian mechanosensitive channels. Notably, a recent *in vivo* ultrasound
590 neuromodulation study of the murine sciatic nerve at 4 MHz, found that tissue displacement *in*
591 *vivo* was highly correlated with the neuromodulation effects (Lee et al., 2020). Nonetheless,

592 additional data or theoretical advances would be required to firmly associate these capacitive
593 transients with changes in membrane tension. If such an association could be made, it would
594 provide strong evidence that ultrasound modulates action potential firing through mechanical
595 effects of radiation force in our experiments. At present, our results do not rule out this idea,
596 but the case for mechanical effects remains speculative, while the role of thermal effects seems
597 highly plausible. Nonetheless, our simulation results support the conclusion that both inhibitory
598 and excitatory effects of high-frequency ultrasound on action-potential firing are due to
599 activation of thermo- and mechanosensitive K2P channels.
600
601 **DISCUSSION**
602 To summarize, the neurophysiological effects of ultrasound that we have described here can all
603 be explained by activation of a sustained outward current. We argue that the molecular basis of
604 this outward current is most likely one or more of the K2P channels expressed by CA1
605 pyramidal neurons. Although a variety of voltage-dependent K^+ currents shape the action-
606 potential waveform and regulate excitability in these neurons, several arguments suggest that
607 K2P channels are the molecular basis of the ultrasound-activated outward conductance. First,
608 the K2P channels TREK and TRAAK, being strongly mechanosensitive and thermosensitive, have
609 biophysical properties that make them especially sensitive to physical effects of ultrasound.
610 Second, the fact that ultrasound has similar effects on firing frequency whether it is applied 500
611 ms before or 1 s after the start of a current step suggests that ultrasound affects firing through
612 a channel that does not undergo prolonged voltage-dependent inactivation during sustained
613 depolarizations. Finally, the neurophysiological effects of ultrasound are, strikingly, essentially

614 the opposite of those caused by knock-out of K2P channels in other neurons, as detailed in the
615 following paragraph.

616 Knock-out of TASK-3 channels in cerebellar granule neurons increased excitability at low
617 input currents, but decreased excitability at high input currents and led to failure of sustained
618 high-frequency firing (Brickley et al., 2007). In addition, knock-out of TASK-3 decreased the
619 maximum firing frequency and decreased action-potential height while increasing action
620 potential width through decease in the rates of both action-potential rise and fall. Similarly,
621 double knock-out of TASK-1 and TASK-3 in hypothalamic hypocretin/orexin neurons inhibited
622 high-frequency action potential firing, reduced the rates of action-potential rise and fall, and
623 decreased the depth of the AHP (Gonzalez et al., 2009). The connection between our results
624 and these knock-out studies is supported by experiments in a heterologous model system
625 consisting of HEK cells transfected with TREK-1 and TASK-3 (with endogenous K_V channels
626 blocked) and Na_V channels simulated by dynamic clamp (MacKenzie et al., 2015). In this model
627 system, high levels of K2P expression were necessary for repetitive action potential firing, and
628 increased K2P conductance increased the rates of action-potential rise and fall and increased
629 the threshold current for action-potential firing. (In the context of this model system, a 74%
630 potentiation of the K2P conductance by halothane produced effects on the rates of rise fall of
631 the same order as we see here, potentially providing an estimate of the potentiation of K2P
632 conductance by ultrasound in our experiments. However, caution should be used in
633 extrapolating from this heterologous model system to neurons expressing a considerably more
634 complex array of ion channels.) Finally, TREK-1 and TRAAK channels are also necessary for high
635 frequency firing at the nodes of Ranvier of afferent neurons (Kanda et al., 2019).

636 Ultrasound neuromodulation has been studied in vertebrate axon preparations, where
637 it has generally been found that ultrasound inhibits action-potential conduction, with the effect
638 specifically attributed to heating in some cases (Young and Henneman, 1961; Mihran et al.,
639 1990; Tsui et al., 2005; Colucci et al., 2009). These results are consistent with the idea that
640 activation of K2P channels by ultrasound can inhibit action potential firing, but it would be
641 worthwhile to revisit these experiments to see whether the bidirectional, spike-frequency-
642 dependent effect that we observe is also present in such preparations. Our results also suggest
643 an approach to ultrasound neuromodulation in which action potential propagation is the locus
644 of neuromodulation, targeting white-matter tracts instead of soma-dense gray matter. The idea
645 that ultrasound-activated K^+ currents can both inhibit and potentiate firing might also help
646 explain why ultrasound can both inhibit and potentiate neural activity *in vivo* (Min et al., 2011).
647 Although activation of K2P channels is sufficient to explain our results, we do not rule
648 out the possibility that ultrasound affects other channels in addition to K2P's; indeed, we think
649 it is likely that ultrasound does affect other channels to some extent. All ion-channel gating
650 reactions are sensitive to temperature, with typical Q10 values of ~3, such that their rates
651 would be expected to increase by about 10% based on the temperature changes in our
652 simulations (Hille, 2001). Mechanical effects of radiation force could also affect channels
653 besides K2P channels. The mechanically gated channel Piezo2 is expressed in a subset of CA1
654 pyramidal neurons (Wang and Hamill, 2020). Piezo1 (Qiu et al., 2019) and TRP channels (Oh et
655 al., 2020; Yoo et al., 2020) have been experimentally linked to ultrasound neuromodulation
656 effects. In addition, most ion channels and membrane proteins, while not functioning
657 physiologically as mechanoreceptors, are sensitive to mechanical stimuli to some extent, either

658 through the energetics of their interactions with hydrophobic core of the lipid bilayer or
659 through mechanical interactions with the cytoskeleton or extracellular matrix. In fact, gating of
660 voltage-dependent Na^+ (Morris and Juranka, 2007), K^+ (Tabarean and Morris, 2002; Laitko and
661 Morris, 2004; Beyder et al., 2010), and Ca^{2+} (Calabrese et al., 2002) channels, and of NMDA
662 receptor channels (Kloda et al., 2007), can be modulated by membrane stretch in membrane
663 patches. However, we previously were unable to detect any mechanical modulation of
664 heterologously expressed NaV1.2 channels by ultrasound at 43 MHz and 90 W/cm^2 under
665 conditions where ultrasound activated the mammalian mechanoreceptor channel Piezo1
666 (Prieto et al., 2018). Neural Na_V channels and KCNQ channels interact with the periodic actin
667 cytoskeleton of axons through spectrin and ankyrin-G at the axon initial segment and nodes of
668 Ranvier and (Zhou et al., 1998; Pan et al., 2006; Leterrier, 2018), suggesting that they may be
669 sensitive to modulation by cytoskeletal tension due to acoustic radiation force. The
670 concentration of TREK-1 and TRAAK channels at the nodes of Ranvier suggest that some similar
671 interaction with the cytoskeleton may be involved in the localization of these channels,
672 although this has not been demonstrated, and the intracellular domains that would facilitate
673 such interactions are relatively small in K2P channels. Ultrasound has been shown to cause
674 changes in cytoskeletal structure (Mizrahi et al., 2012), which might also affect the activity of
675 cytoskeleton-associated channels. Thus investigation of the role of other ion channels in
676 ultrasound neuromodulation should continue. Notably, several of the channels discussed above
677 have roles in synaptic transmission, so effects of ultrasound on these channels would not be
678 revealed by our experiments on somatic excitability in response to injected current.

679 It is well established that high-intensity light at infrared and shorter wavelengths can
680 modulate neural activity through tissue heating. As a general principle, thermal
681 neuromodulation effects in response to optical stimulation would be expected to be very
682 similar to thermal neuromodulation effects caused by ultrasound, and studies of optical
683 neuromodulation could therefore provide useful guidance in interpreting our results. However,
684 optically based thermal neuromodulation experiments are highly heterogeneous in terms of the
685 neuromodulation effect, the temperature rise required to produce the effect, and the
686 mechanistic interpretation of the results (Wells et al., 2007; Richter et al., 2011; Shapiro et al.,
687 2012; Duke et al., 2013; Walsh et al., 2016; Lothet et al., 2017; Paris et al., 2017; Owen et al.,
688 2019; Zhu et al., 2019), so their usefulness is limited in this respect. Both inhibition and
689 potentiation of firing have been reported, and the increase in temperature has varied
690 considerably, ranging from less than 1 C to 10's of degrees C. The temperature rise in our
691 simulations is on the low end of this range. However, it has been proposed that spatial or
692 temporal gradients in temperature, rather than the absolute temperature change, may
693 determine the response to thermal stimuli (Wells et al., 2007; Paris et al., 2017). In addition,
694 heating can cause phase changes in lipid bilayers, which have been shown to modulate ion
695 channel activity (Seeger et al., 2010); in this case, the response to heating would also depend
696 critically on the initial temperature. Interestingly, a recent study demonstrated inhibition of
697 firing by small (2°C or less) increases in temperature in several different types of neurons, but
698 *not* in CA1 pyramidal neurons (Owen et al., 2019). These effects were attributed to inward
699 rectifier (K_{ir}) potassium channels, which are not expressed in CA1 pyramidal neurons. However,
700 our results suggest that the lack of an effect in pyramidal neurons could also be explained if the

701 experiments were performed at a point on the f-i curve where competing inhibitory and
702 excitatory effects of heat-activated K^+ current result in no net effect on firing frequency. A
703 recent *in vivo* ultrasound neuromodulation study in a rat model using ultrasound at 3.2 MHz
704 with exceptionally long ultrasound exposure times (10's of seconds; see below for a more
705 general discussion of *in vivo* ultrasound neuromodulation studies) also found that inhibition
706 could be produced by ultrasound-induced temperature rises of 2°C or less (Darrow et al., 2019),
707 consistent with this result and our results.

708 Finally, a critical question—to which we cannot yet provide a definitive answer—is
709 whether the mechanisms underlying the neuromodulatory effects of ultrasound are the same
710 in our experiments and in *in vivo* experiments using low frequencies. Two results that strongly
711 argue against similar mechanisms are the much lower intensities that have been reported to
712 cause neuromodulatory effects in some low-frequency, *in vivo* experiments in small animal
713 models (Tufail et al., 2010) as compared with our results, and the apparent increase in efficacy
714 of ultrasound neuromodulation at lower frequencies in *in vivo* experiments. Both thermal and
715 radiation force effects are proportional to ultrasound intensity, and to the ultrasound
716 attenuation coefficient, which in tissue is proportional to frequency raised to the power of ~1.1
717 (Hand, 1998), so these effects would generally be smaller in *in vivo* experiments (especially
718 small animal experiments) as compared with our experiments. Compounding this issue is the
719 fact that opposite dependences on the ultrasound frequency have been observed in *in vivo* and
720 *in vitro* experiments. In an *in vivo* mouse model of ultrasound neuromodulation, it was
721 determined that the efficacy of neuromodulation decreased with increasing frequency over the
722 range 0.25-2.9 MHz (King et al., 2013; Ye et al., 2016). This frequency dependence is the

723 opposite of what would be expected for either a thermal or radiation force mechanism. In
724 contrast, Menz et al. (2019) found that the efficacy of neuromodulation increases with
725 frequency over the range 1.9-43 MHz in the retina *in vitro*, a thin neural tissue preparation
726 similar to the one used in our experiments. However, they proposed a model to explain this
727 discrepancy. Lower ultrasound frequencies generally result in a larger stimulated tissue volume,
728 which could translate into a more effective stimulus for certain structures of circuit-level neural
729 connectivity, despite a weaker effect of low-frequency ultrasound at the level of an individual
730 cell. (The model was presented in the context of a radiation force mechanism, but the same
731 principle could apply for a thermal mechanism). The idea that circuit-level mechanisms can
732 amplify the response to ultrasound is supported by comparison of our results with the response
733 to ultrasound in the retina at 43 MHz. In the retina, potentiation of action-potential firing by
734 ultrasound at 43 MHz saturates at 10 W/cm^2, as measured at the population level in an intact,
735 active neural circuit. Although we have not performed a detailed investigation of the intensity
736 dependence, we find that a much higher intensity, 50 W/cm^2, produces relatively moderate
737 effects on excitability in single cells in the absence of significant network activity. Focusing
738 solely on the local, cell-level amplitude of thermal and radiation force effects may therefore
739 overlook important factors related to the global, network-level distribution of these effects.
740 Such considerations may eliminate the differences in effective ultrasound parameters for *in*
741 *vivo* and *in vitro* experiments as an argument against similar physical mechanisms for
742 neuromodulation by high- and low-frequency ultrasound.
743 In conclusion, our results demonstrate that high-frequency ultrasound is a viable and
744 promising modality for neuromodulation applications where frequency is not limited by

745 transmission through the skull, and our insights into the common molecular mechanisms
746 underlying both inhibitory and excitatory effects of high-frequency ultrasound pave the way for
747 rational design and optimization of neuromodulation protocols to consistently produce either
748 inhibitory or excitatory effects.
749

750 **ACKNOWLEDGMENTS**

751 We thank the PIs and members of the Baccus, Butts-Pauly and Huguenard laboratories for
752 helpful discussions. We thank Mike Menz and Stephen Baccus for critically reading the
753 manuscript. We thank Marianna Kiraly, Dong Li, and Jason Clark for help with hippocampal slice
754 preparation and recording. We thank the Stephen Boxer lab for sharing their plasma cleaner.

755 This work was supported by NIH R01 EB019005 (M.M. and B.K.Y.) and NIH BRAIN initiative R01
756 NS11215 (M.M. and B.K.Y.).

757 The authors declare no competing financial interests.

758 **AUTHOR CONTRIBUTIONS**

759 Martin Prieto performed experiments, analyzed data, and wrote the manuscript. Martin Prieto
760 and Kamyar Firouzi performed computational modeling. Merritt Maduke, Daniel Madison, and
761 Butrus Khuri-Yakub supervised research. All authors contributed to the design and
762 interpretation of experiments and edited and revised the manuscript.

763

764 **Table 1. Values of Material Properties Used in Finite-Element Simulations.**

	water	polystyrene	brain tissue
density (kg/m^3)	1000[a]	1040[b]	1007[c]
speed of sound (m/s)	1500[a]	2300[b]	1538[c]
attenuation coefficient at 43 MHz (neper/m)	46[d]	160[e]	253[f]
heat capacity (J/kg·K)	4180[a]	1200[g]	3500[h]
thermal conductivity (W/m·K)	0.6[a]	0.1[g]	0.5[h]
Young's modulus (Pa)	(not applicable)	10^9 [i]	500[j]
Poisson's ratio	(not applicable)	0.4[i]	0.4998[k]
shear viscosity (Pa·s)	(not applicable)	(not applicable)	1[l]

765 Sources for material properties are as follows: [a]standard value; [b]based on typical acoustic
766 properties of plastics (Selfridge, 1985); [c]following Menz et al. (2019), based on (Thijssen et al.,
767 1985); [d] (Company, 1965); [e]measured (Prieto et al., 2018); [f]following Menz et al. (2019), based
768 on (de Korte et al., 1994); [g]based on typical thermal properties of plastics (Gaur and
769 Wunderlich, 1982; Harper, 2006); [h]typical values for soft tissues (Hand, 1998); [i]based on typical
770 mechanical properties of plastics (Harper, 2006); [j]Menz et al. (2019), from measurements of
771 ultrasound-induced displacement in the retina; [k]tissue assumed to be incompressible for small
772 deformations; [l]see text.

773

774

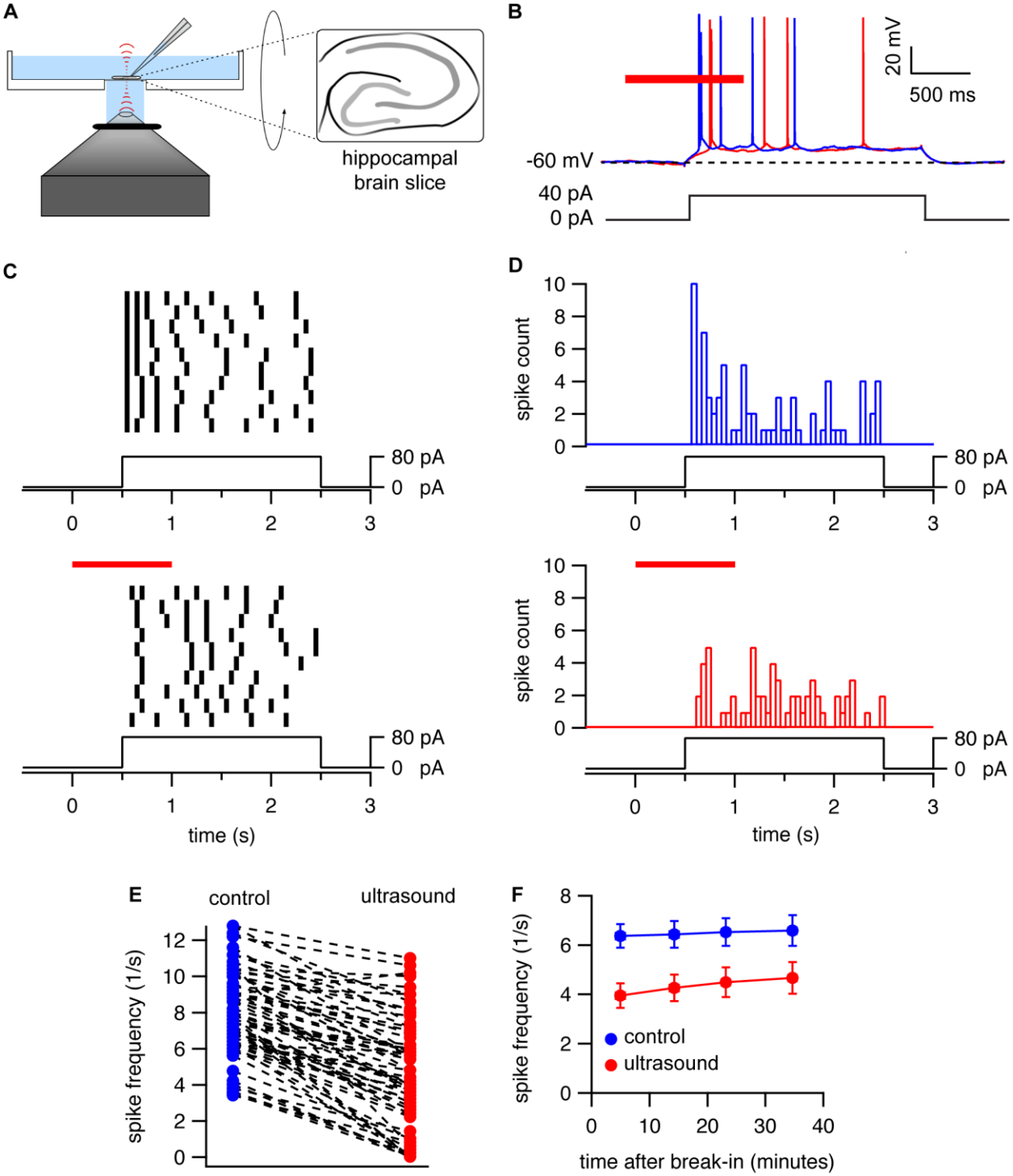

Figure 1. Consistent inhibition of action potential firing by high-frequency ultrasound. A. Diagram of experimental set-up. Ultrasound is applied to 500-micron hippocampal brain slices resting on a 25-micron film of polystyrene. The 43-MHz focused transducer is located below the experimental chamber, with ultrasound propagating perpendicular to the bottom of the recording chamber. **B.** Experimental protocol and example voltage traces showing inhibition of

action potential firing by ultrasound. A 1-s, continuous-wave ultrasound pulse at 43 MHz and 50 W/cm^2 (*red bar*) is applied 500 ms before the start of a 2-s current injection. Voltage traces are shown in the presence (*red*) and absence (*blue*) of the ultrasound stimulus. The *dashed line* indicates the resting membrane voltage. **C.** Example raster plots showing a consistent effect of ultrasound on firing frequency. The results of twenty consecutive trials of the protocol in panel B, alternating between the control (*top*) and ultrasound (*bottom*) conditions, are shown. The voltage traces were divided into 50-ms bins; a solid black bin indicates that an action potential occurred within that particular time bin. Time is relative to the start of the ultrasound pulse. **D.** Spike-time histograms prepared by summing the ten trials for the control (*top, blue bars*) and ultrasound (*bottom, red bars*) conditions from panel C. **E.** Summary of the effects of ultrasound for N = 66 cells. The average firing frequency during the first 500 ms of the current step is shown for the control (*blue*) and ultrasound (*red*) conditions. **F.** Stability of the ultrasound response. Mean (±SEM, N = 10 cells) spike frequencies during the first 500 ms of a current step in the presence (*red circles*) and absence (*blue circles*) of ultrasound for the protocol shown in panel B, as a function of time relative to break-in (establishment of whole-cell recording configuration). Spike frequencies were measured at various time points between 0 and 10, 10 and 20, 20 and 30, and 30 and 40 minutes after break-in. The x-values represent the mean start time for the protocol to measure spike frequencies (which comprised 2 minutes of recording time). The amplitude of the current step was adjusted over time to maintain spiking behavior as close as possible to that at the start of the experiment.

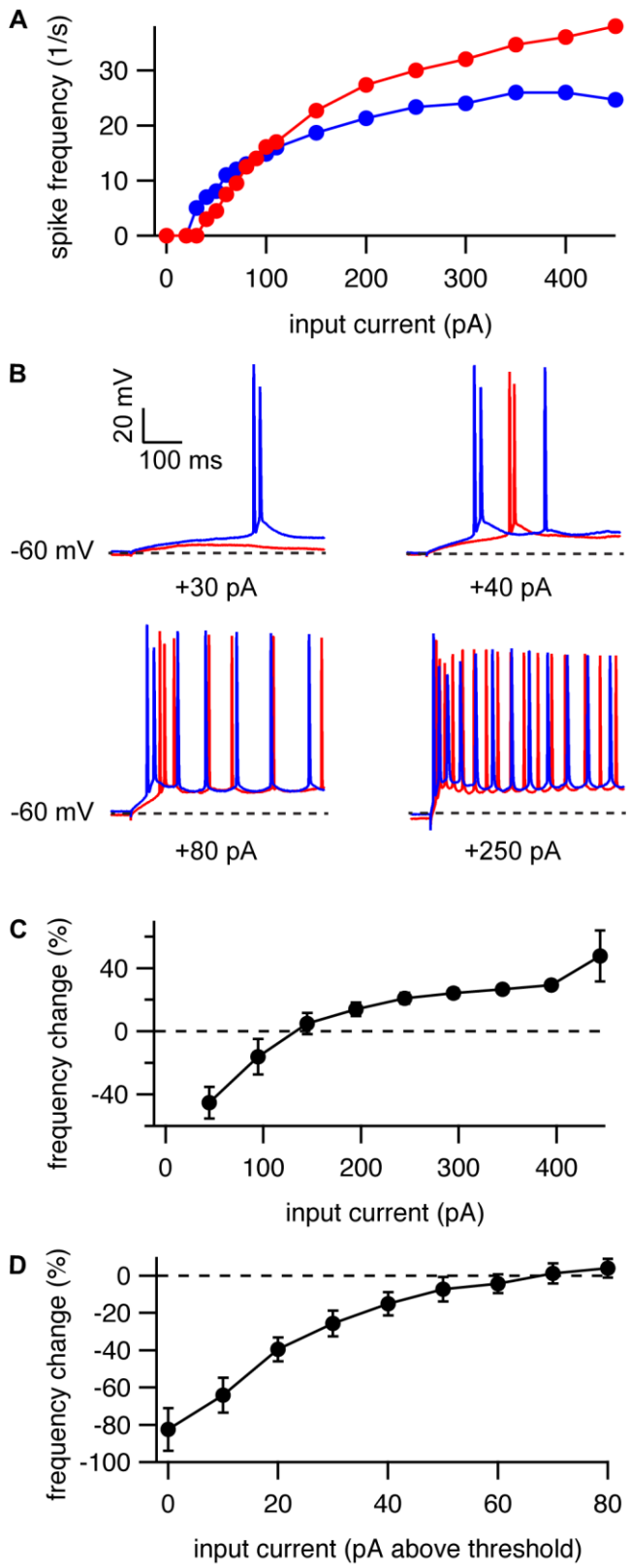
A
spike frequency (1/s)
30
20
10
0
0
100
200
300
400
input current (pA)
B
20 mV
100 ms
-60 mV
+30 pA
+40 pA
-60 mV
+80 pA
+250 pA
C
frequency change (%)
40
0
-40
0
100
200
300
400
input current (pA)
D
frequency change (%)
0
-20
-40
-60
-80
-100
0
20
40
60
80
input current (pA above threshold)

803

Figure 2. Ultrasound can inhibit or potentiate action-potential firing. A. Example frequency-input curve showing average firing frequency during the first 500 ms of a current step as a function of input current, with (*red*) and without (*blue*) a 1-s ultrasound pulse starting before 500 ms before the start of the current step. Each point represents the average of three trials on the same cell. **B.** Example voltage traces for the cell in A showing action potential firing during the first 500 ms of current steps to either +30, +40, +80, or +250 pA, with (*red*) and without (*blue*) ultrasound. The *dashed lines* indicate the approximate resting membrane voltage of -60 mV. **C.** Mean (±SEM, N = 9 cells) change in spike frequency in response to ultrasound as a function of input current. **D.** Inhibition is strongest near threshold. Mean (±SEM, N = 7 cells) change in spike frequency in response to ultrasound as a function of input current relative to the threshold current for action potential firing, for near-threshold currents.

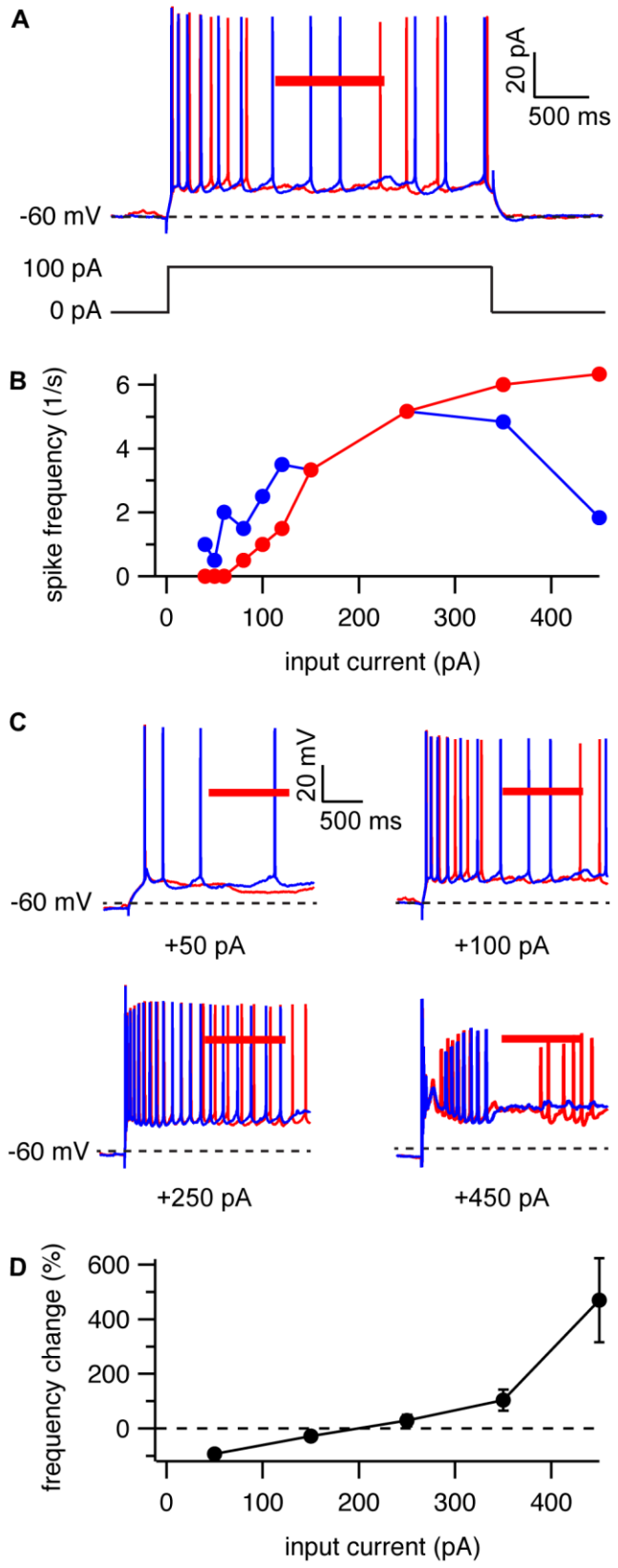
A
20 pA
500 ms
-60 mV
100 pA
0 pA
B
spike frequency (1/s)
6
4
2
0
0
100
200
300
400
input current (pA)
C
20 mV
500 ms
-60 mV
+50 pA
+100 pA
-60 mV
+250 pA
+450 pA
D
frequency change (%)
600
400
200
0
0
100
200
300
400
input current (pA)

816

817 **Figure 3. Ultrasound can also inhibit or potentiate action-potential firing when applied late in**
818 **a current step. A.** Experimental protocol and example voltage traces with (*red*) and without
819 (*blue*) ultrasound. Ultrasound is applied 1 s after the start of a 3-s current step. The *dashed line*
820 indicates the resting membrane voltage. **B.** Example frequency-input curve showing average
821 firing frequency during the ultrasound application for the protocol in A (*red*) and during the
822 same time window without ultrasound (*blue*), as a function of input current. Each point
823 represents the average of three trials on one cell. **C.** Example voltage traces for the cell in B
824 showing action potential firing during the ultrasound application (*red*) and during the same
825 time window without ultrasound (*blue*) in response to current steps to either +50, +100, +250,
826 or +450 pA. The *dashed lines* indicate the approximate resting membrane voltage of -60 mV. **D.**
827 Mean (±SEM) change in spike frequency in response to ultrasound as a function of input current
828 (N = 3 cells at +50 pA; N = 6 cells at all other input currents). (In 3 cells, the firing frequency at
829 +50 pA was zero for both the control and ultrasound conditions).
830

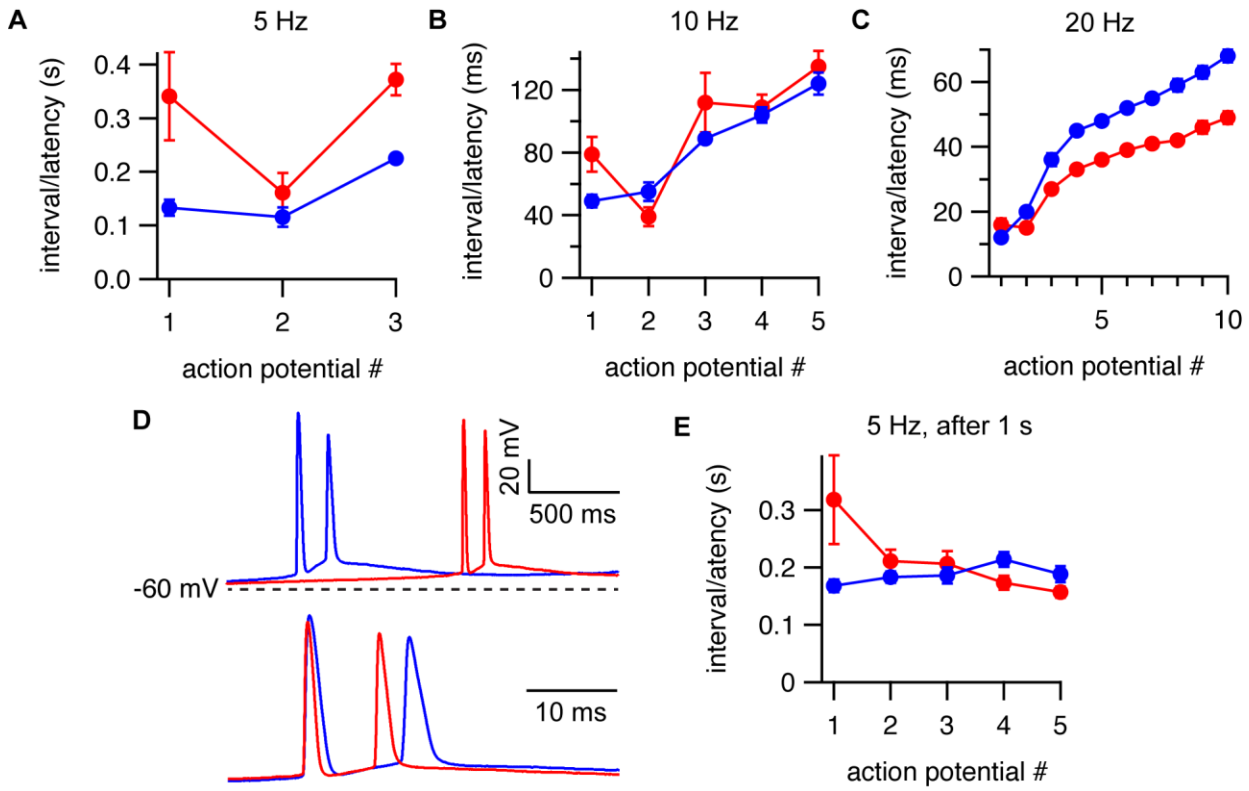

Figure 4. Effects of ultrasound on action potential timing. A-C. Mean (±SEM) latency between the start of the current step and the first action potential, and mean intervals between the first and second, and second and third, etc. action potentials, for cells firing at average frequencies of approximately 5 Hz (N = 13 cells), 10 Hz (N = 15 cells), and 20 Hz (N = 13 cells) during the first 500 ms of the current step, with (*red*) or without (*blue*) a 1-s ultrasound pulse starting 500 ms before the current step. The actual spike frequencies were 5.6 ± 0.1, 10.5 ± 0.2, and 20.4 ± 0.3 Hz, and the injected currents were 70 ± 7, 115 ± 9, and 292 ± 28 pA for the 5, 10, and 20 Hz conditions. **D.** Example voltage traces showing decreased interval between the first and second action potentials at low average firing frequency. The top panel shows the first two action potentials for the control (*blue*) and ultrasound (*red*) conditions. The *dashed line* indicates the approximate resting membrane voltage of -60 mV. The bottom panel shows the same data, aligned to the action potential threshold on a zoomed-in time scale. **E.** Same as A-C, for an

average firing frequency of 5 Hz, except that ultrasound was applied 1-s after the start of a 3-s current step, and the average firing frequency and intervals/latency were determined during ultrasound stimulus or during the same time period without ultrasound (N = 6). The actual spike frequency was 5.2 ± 0.2 Hz, and the injected currents was 183 ± 21 pA.

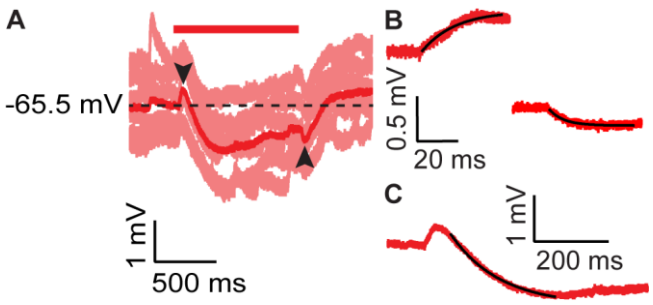

848

849 **Figure 5. Effects of ultrasound on resting membrane potential and membrane capacitance. A.**
850 Six individual voltage traces (*pink*) and the average of these voltage traces (*red*) showing the
851 effect of ultrasound (*red bar*) on resting membrane potential. The *black arrows* indicate
852 transients due to changes in membrane capacitance. The *dashed line* indicates the mean resting
853 membrane voltage. **B.** Zoomed-in timescale showing the fast voltage transients (*black arrows*
854 in A) for ultrasound onset (*top left*) and offset (*bottom right*). Exponential fits (*black lines*) to the
855 rise and fall of the voltage transients give amplitudes and time constants of 0.45 mV and 16.3
856 ms for the onset and 0.22 mV and 6.7 ms for the offset, for the example shown; mean values
857 (±SEM) were 0.41 ± 0.04 mV and 10.4 ± 1.2 ms for the onset and 0.35 ± 0.04 mv and 9.7 ± 1.7
858 ms for the offset (N = 15). No significant differences were found between the time constants (P
859 = 0.73) or the amplitude (P = 0.087) of the transients (paired, two-tailed Student's t-tests) **C.**
860 Slow membrane hyperpolarization in response to ultrasound from the average trace in panel A
861 on a zoomed-in scale, along with an exponential fit (*black line*) to the initial hyperpolarization.
862 The amplitude and time constant of the exponential fit were 1.55 mV and 132 ms for the
863 example shown; mean values (±SEM) were 2.4 ± 0.3 mV and 173 ± 18 ms (N = 15).

864

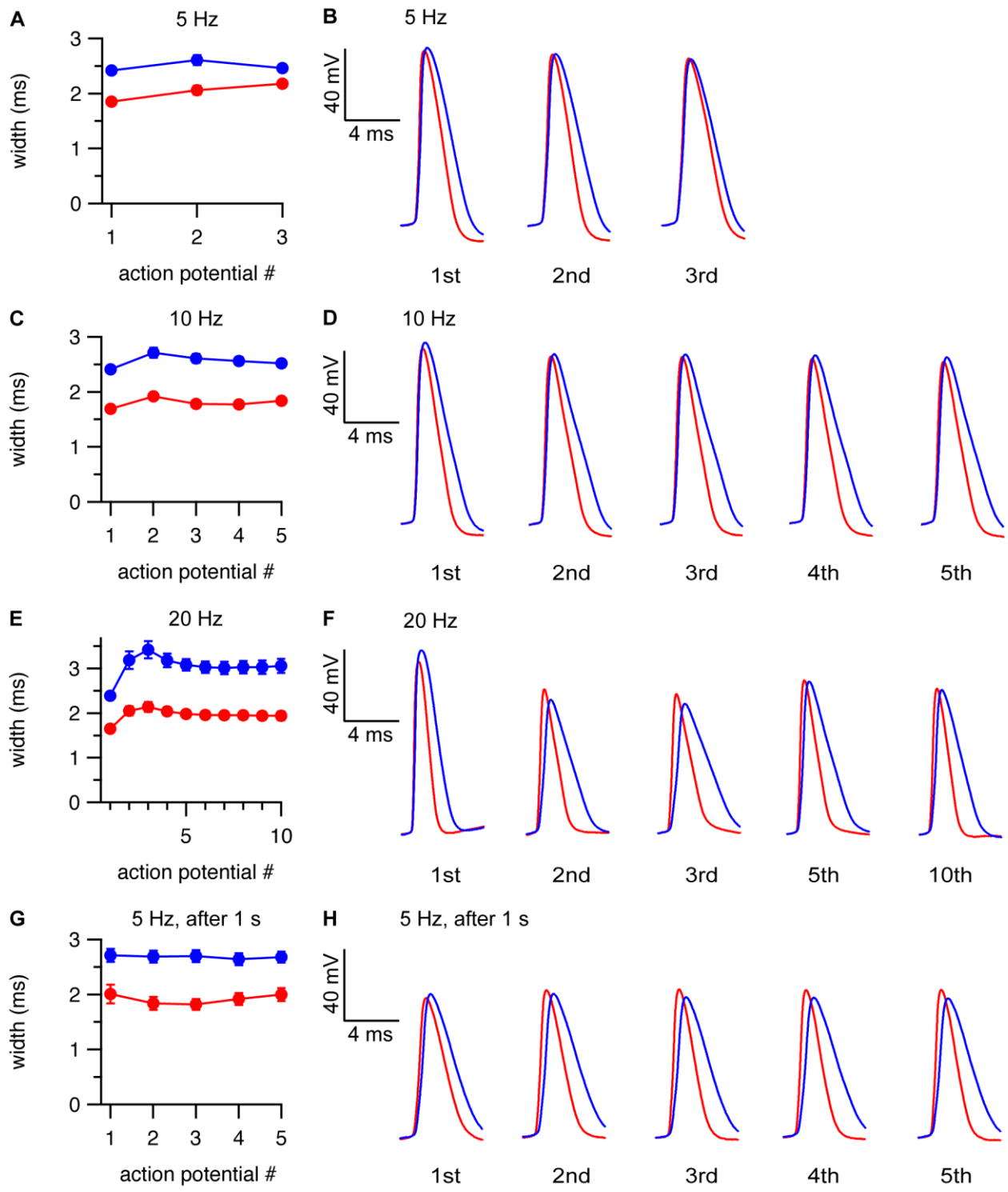

Figure 6. Ultrasound decreases action-potential width. A-B. Mean (±SEM, N = 13 cells) action-potential widths (A) and example action-potential waveforms aligned to the action-potential threshold (B) as function of action-potential number in the presence (*red*) and absence (*blue*) of a 1-s ultrasound pulse starting 500 ms before the current step, for cells firing at an average firing frequency of approximately 5 Hz (as measured during the first 500 ms of the current step)

in the control condition. **C-D.** As in A-B, but for cells firing at an average firing frequency of approximately 10 Hz in the control condition (N = 15). **E-F.** As in A-B, but for cells firing at an average firing frequency of approximately 20 Hz in the control condition (N = 13). **G-H.** As in A-B, but with ultrasound applied 1 s after the start of a 3-s current step, for cells firing at an average firing frequency of approximately 5 Hz in the control condition, with firing frequency determined in a 1-s window starting 1 s after the current step (corresponding to the time period of the ultrasound stimulus), and action potential number relative to the start of the ultrasound stimulus (N = 6).

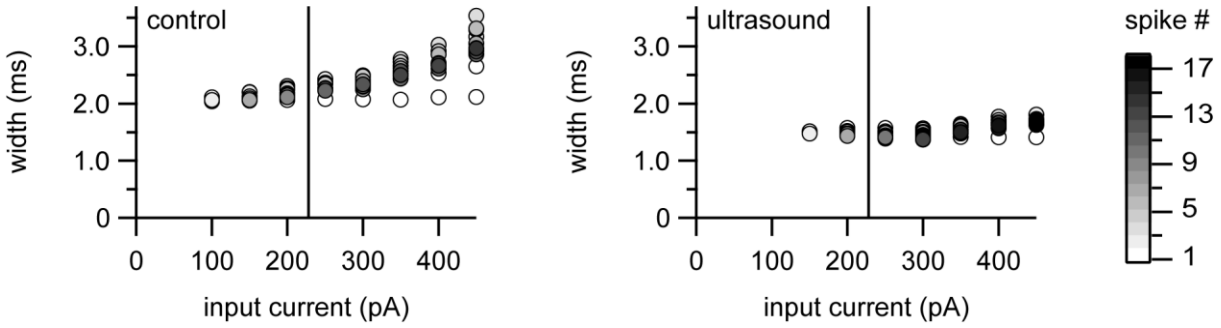

Figure 7. Ultrasound reduces action-potential broadening. Example data showing action-potential width as a function of action-potential number (indicated in *grayscale*, scale bar at far left) and input current level, for the first 500 ms of the current step, for currents from 0 to +450 pA in 50 pA steps, with (*right*) or without (*left*) a 1-s ultrasound pulse starting 500 ms before the current step. The vertical lines indicate the approximate location of the transition between inhibitory and potentiating effects of ultrasound.

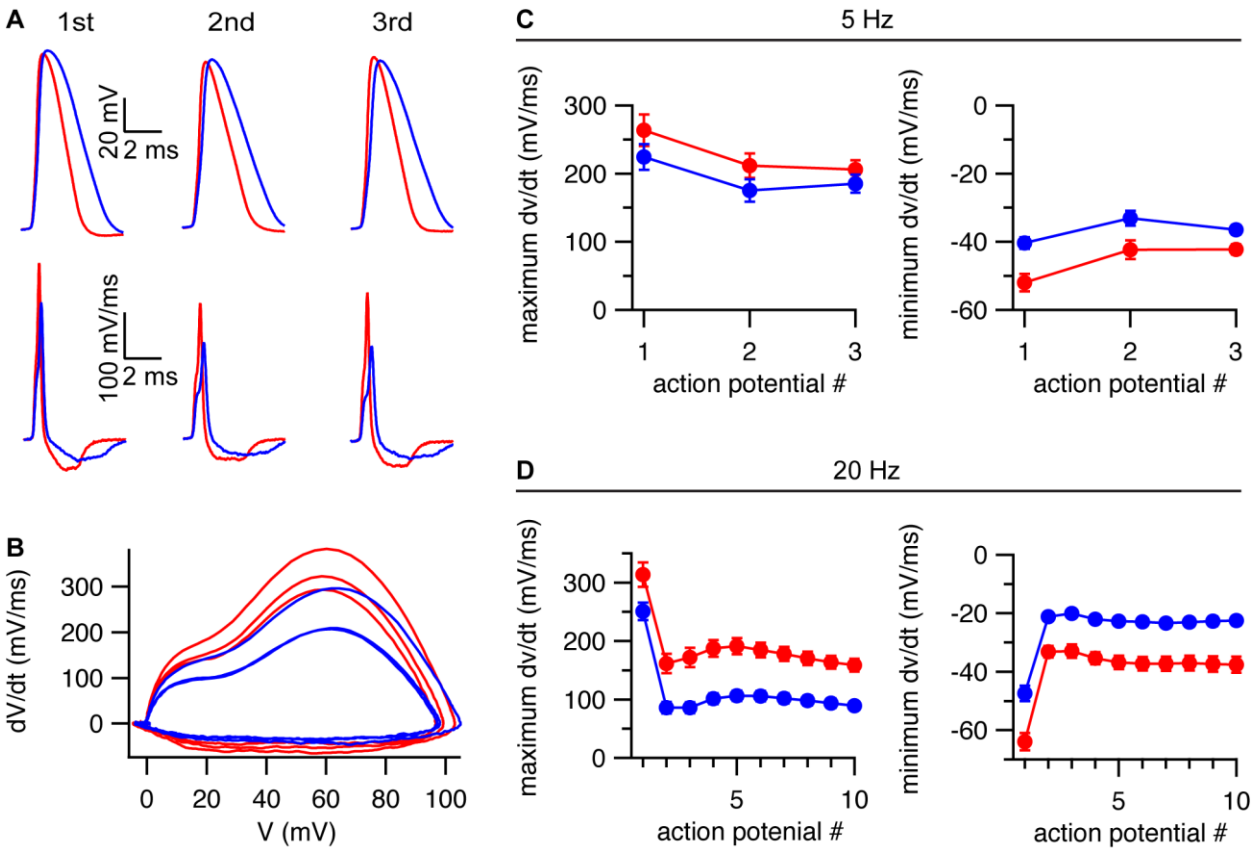

Figure 8. Effects of ultrasound on depolarization and repolarization rates. A. Example traces showing the membrane voltage (*top*) and its first derivative (*bottom*) for the first three action potentials in response to a +100 pA current step in the presence (*red*) and absence (*blue*) of a 1-s ultrasound pulse starting 500 ms before the current step, aligned to the action potential threshold. **B.** Phase plots for the action potentials shown in panel A. **C-D.** Maximum rates of depolarization (*left)* and repolarization (*right*) during the action potential (mean ± SEM, N = 13 cells), as a function of action potential number, in the presence (*red*) and absence (*blue*) of a 1-s ultrasound pulse starting 500 ms before the current step, for cells firing at an average firing frequency of 5 Hz (**C**) or 20 Hz (**D**) in the control condition.

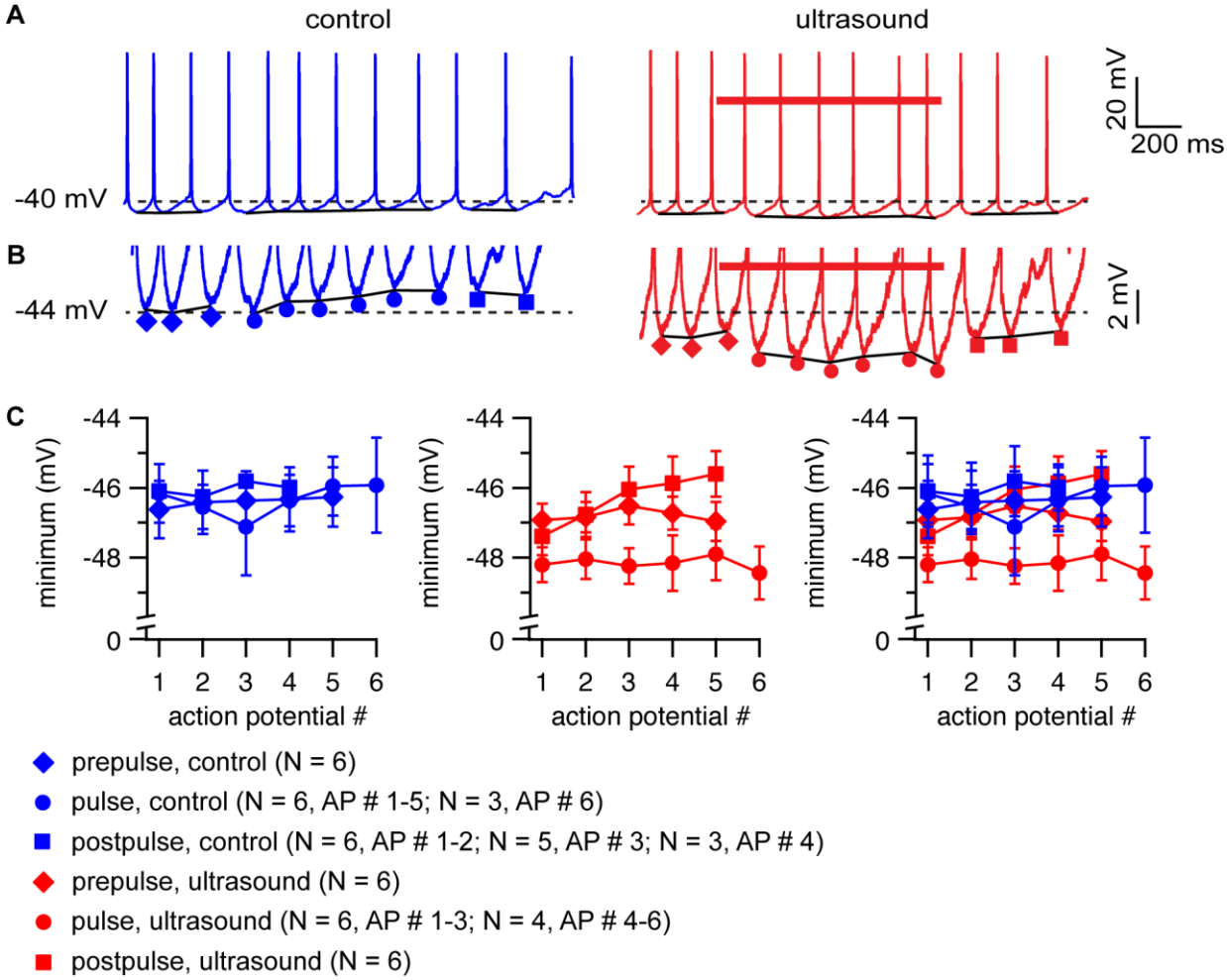

Figure 9. Ultrasound increases the depth of the afterhyperpolarization. A. Example voltage traces comparing voltage minima between action potentials in response to a 3-s, 250-pA current step with (*red voltage trace, right*) and without (*blue voltage trace, left*) a 1-s ultrasound pulse (*red bar*) starting 1 s after the start of the current step. The *solid black lines* connect the voltage minima between action potentials before, during, or after the ultrasound pulse, or during the corresponding time periods for the control condition. The dashed lines indicate a reference voltage level of -40 mV. The resting membrane voltage for this cell was -63 mV. **B.** Same as panel A, on a zoomed-in voltage scale. The *red diamonds* indicate voltage minima before the ultrasound pulse, *red circles* indicate voltage minima during the ultrasound pulse, and *red squares* indicate voltage minima following the ultrasound pulse; *blue symbols* indicate voltage minima for the corresponding time periods for the control condition. The dashed lines indicate a reference voltage level of -44 mV. **C.** Mean (±SEM, N = 3-6 cells, see figure panel for details) values of the voltage minimum, as a function of action potential (AP) number for the first four to six action potentials before, during, and after the ultrasound pulse, along with the equivalent mean values for the control condition, following the symbolism indicated in panel B. The means were determined for cells firing at the same average frequency

(5 Hz) during a 1-s window starting 1 s after the start of the current step (corresponding to the period of the ultrasound stimulus) in the control condition. For clarity, the results are shown separately for the control group only (*left*), the ultrasound group only (*middle*), and for both groups simultaneously (*right*). Significant differences between groups were only found in the presence of ultrasound ($P = 1.0 \times 10^{-4}$, 1.4×10^{-5}, and 0.16 for before versus during, during versus after, and before versus after the ultrasound pulse; P = 0.92, 0.39, and 0.35 for comparisons of the same time periods in the control condition (unpaired, two-tailed Student's t-tests, unequal variance).

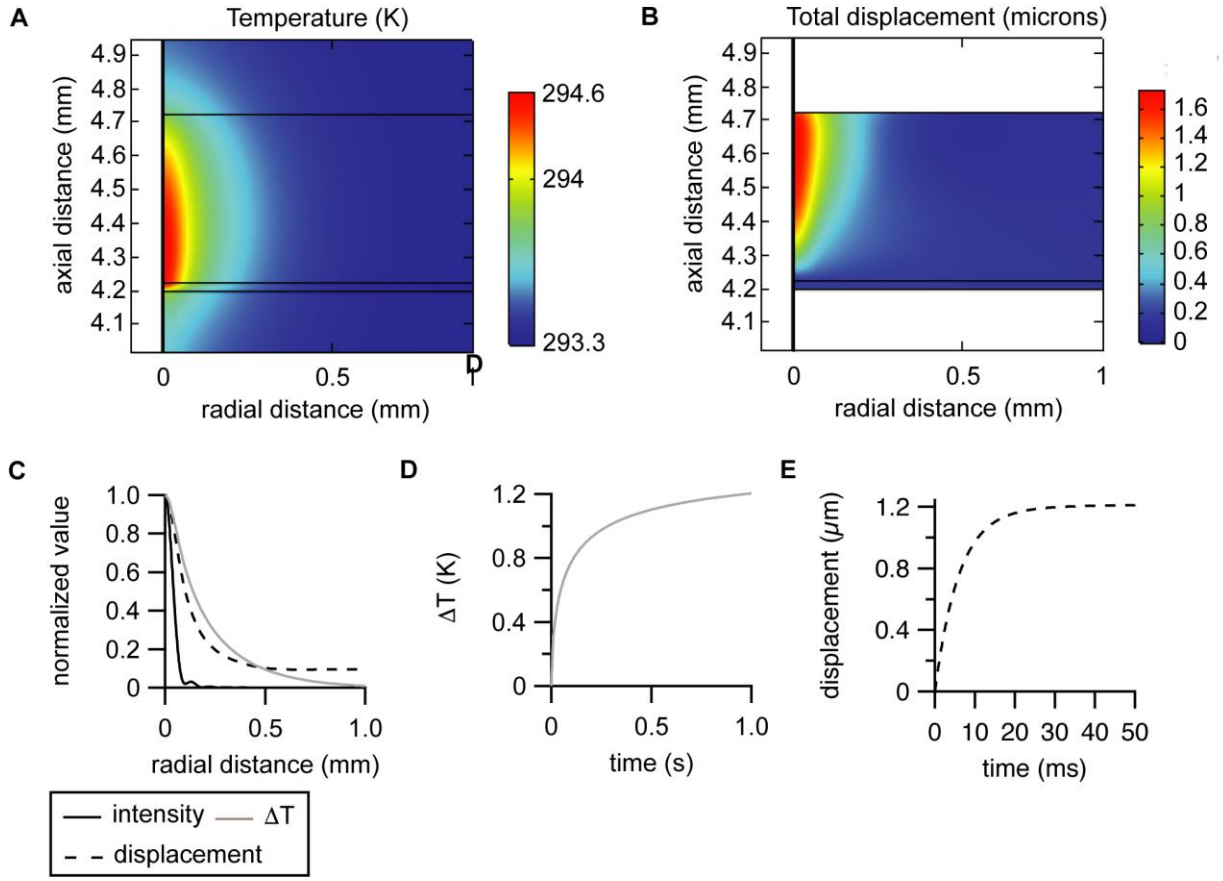

Figure 10. Simulated tissue heating and displacement in response to ultrasound. A. Spatial profile of temperature after one second of ultrasound exposure at 43 MHz and 50 W/cm^2, as a function of axial distance from the transducer surface and radial distance from the ultrasound beam axis, in a 500-micron thick brain slice and 25-micron thick polystyrene film (*middle two layers*) and the surrounding fluid (external solution, *top layer*, and distilled water, *bottom layer*). **B.** Spatial profile of the static total displacement in response to acoustic radiation force in the brain slice and polystyrene film. **C.** Normalized values of the acoustic intensity (*solid black line*), temperature rise after 1 second of ultrasound exposure (*solid gray line*), and total displacement (*dashed line*), at a depth of 250 microns in the brain slice, as a function of radial distance. **D.** Time course of the temperature rise in response at ultrasound at a depth of 250

microns in the brain slice on the axis of the ultrasound beam. The time course of the temperature change can be described by two exponential components with amplitudes and time constants of -0.56 C and 30 ms, and -0.57 C and 295 ms, for a weighted time constant of 164 ms. **E.** Time course of the displacement in response at ultrasound at a depth of 250 microns in the brain slice on the axis of the ultrasound beam. The time course of the displacement change can be described by two exponential components with amplitudes and time constants of -1.2 microns and 6 ms, and -0.13 microns and 344 ms, for a weighted time constant of 39 ms. Note that the steady-state displacement is slightly smaller than in the static displacement simulation due to the inclusion of the fluid loading in the dynamic displacement simulation.

949 Abolfathi, N., A. Naik, M. Sotudeh Chafi, G. Karami, and M. Ziejewski. 2009. A micromechanical
950 procedure for modelling the anisotropic mechanical properties of brain white matter.
951 *Comput Methods Biomech Biomed Engin*. 12:249-262.
952 Alvarez, O., and R. Latorre. 1978. Voltage-dependent capacitance in lipid bilayers made from
953 monolayers. *Biophys J*. 21:1-17.
954 Arbogast, K.B., and S.S. Margulies. 1999. A fiber-reinforced composite model of the viscoelastic
955 behavior of the brainstem in shear. *J Biomech*. 32:865-870.
956 Bean, B.P. 2007. The action potential in mammalian central neurons. *Nat Rev Neurosci*. 8:451-
957 465.
958 Beyder, A., J.L. Rae, C. Bernard, P.R. Strege, F. Sachs, and G. Farrugia. 2010. Mechanosensitivity
959 of Nav1.5, a voltage-sensitive sodium channel. *J Physiol*. 588:4969-4985.
960 Blackmore, J., S. Shrivastava, J. Sallet, C.R. Butler, and R.O. Cleveland. 2019. Ultrasound
961 Neuromodulation: A Review of Results, Mechanisms and Safety. *Ultrasound Med Biol*.
962 45:1509-1536.
963 Blanton, M.G., J.J. Lo Turco, and A.R. Kriegstein. 1989. Whole cell recording from neurons in
964 slices of reptilian and mammalian cerebral cortex. *J Neurosci Methods*. 30:203-210.
965 Brickley, S.G., M.I. Aller, C. Sandu, E.L. Veale, F.G. Alder, H. Sambi, A. Mathie, and W. Wisden.
966 2007. TASK-3 two-pore domain potassium channels enable sustained high-frequency
967 firing in cerebellar granule neurons. *J Neurosci*. 27:9329-9340.
968 Brohawn, S.G., Z. Su, and R. MacKinnon. 2014. Mechanosensitivity is mediated directly by the
969 lipid membrane in TRAAK and TREK1 K+ channels. *Proc Natl Acad Sci U S A*. 111:3614-
970 3619.
971 Brohawn, S.G., W. Wang, A. Handler, E.B. Campbell, J.R. Schwarz, and R. MacKinnon. 2019. The
972 mechanosensitive ion channel TRAAK is localized to the mammalian node of Ranvier.
973 *Elife*. 8.
974 Bystritsky, A., A.S. Korb, P.K. Douglas, M.S. Cohen, W.P. Melega, A.P. Mulgaonkar, A. DeSalles,
975 B.K. Min, and S.S. Yoo. 2011. A review of low-intensity focused ultrasound pulsation.
976 *Brain Stimul*. 4:125-136.
977 Calabrese, B., I.V. Tabarean, P. Juranka, and C.E. Morris. 2002. Mechanosensitivity of N-type
978 calcium channel currents. *Biophys J*. 83:2560-2574.
979 Calhoun, M.A., S.A. Bentil, E. Elliott, J.J. Otero, J.O. Winter, and R.B. Dupaix. 2019. Beyond linear
980 elastic modulus: viscoelastic models for brain and brain mimetic hydrogels. *ACS*
981 *Biomaterials Science & Engineering*. 5:3964-3973.
982 Castaneda-Castellanos, D.R., A.C. Flint, and A.R. Kriegstein. 2006. Blind patch clamp recordings
983 in embryonic and adult mammalian brain slices. *Nat Protoc*. 1:532-542.
984 Colucci, V., G. Strichartz, F. Jolesz, N. Vykhodtseva, and K. Hynynen. 2009. Focused ultrasound
985 effects on nerve action potential in vitro. *Ultrasound Med Biol*. 35:1737-1747.
986 Company, C.R. 1965. Handbook of Chemistry and Physics. 45th.ed. Chemical Rubber Compnay,
987 Cleveland, OH.
988 Cotero, V., Y. Fan, T. Tsaava, A.M. Kressel, I. Hancu, P. Fitzgerald, K. Wallace, S. Kaanumalle, J.
989 Graf, W. Rigby, T.J. Kao, J. Roberts, C. Bhushan, S. Joel, T.R. Coleman, S. Zanos, K.J.
990 Tracey, J. Ashe, S.S. Chavan, and C. Puleo. 2019. Noninvasive sub-organ ultrasound
991 stimulation for targeted neuromodulation. *Nat Commun*. 10:952.

992 Darrow, D.P., P. O'Brien, T.J. Richner, T.I. Netoff, and E.S. Ebbini. 2019. Reversible
993 neuroinhibition by focused ultrasound is mediated by a thermal mechanism. *Brain*
994 *Stimul*. 12:1439-1447.
995 de Korte, C.L., A.F. van der Steen, and J.M. Thijssen. 1994. Acoustic velocity and attenuation of
996 eye tissues at 20 MHz. *Ultrasound Med Biol*. 20:471-480.
997 Downs, M.E., S.A. Lee, G. Yang, S. Kim, Q. Wang, and E.E. Konofagou. 2018. Non-invasive
998 peripheral nerve stimulation via focused ultrasound in vivo. *Phys Med Biol*. 63:035011.
999 Duck, F.A. 1998. Radiation pressure and acoustic streaming. *In* Ultrasound in Medicine. F. Duck,
1000 A. Baker and H. Starritt, editors. Institute of Physics Publishing, Philadelphia, PA.
1001 Duke, A.R., M.W. Jenkins, H. Lu, J.M. McManus, H.J. Chiel, and E.D. Jansen. 2013. Transient and
1002 selective suppression of neural activity with infrared light. *Sci Rep*. 3:2600.
1003 Evans, E.A., R. Waugh, and L. Melnik. 1976. Elastic area compressibility modulus of red cell
1004 membrane. *Biophys J*. 16:585-595.
1005 Fomenko, A., C. Neudorfer, R.F. Dallapiazza, S.K. Kalia, and A.M. Lozano. 2018. Low-intensity
1006 ultrasound neuromodulation: An overview of mechanisms and emerging human
1007 applications. *Brain Stimul*. 11:1209-1217.
1008 Fry, F.J., H.W. Ades, and W.J. Fry. 1958. Production of reversible changes in the central nervous
1009 system by ultrasound. *Science*. 127:83-84.
1010 Gaur, U., and B. Wunderlich. 1982. Heat-Capacity and Other Thermodynamic Properties of
1011 Linear Macromolecules .5. Polystyrene. *J Phys Chem Ref Data*. 11:313-325.
1012 Gavrilov, L.R., E.M. Tsirulnikov, and I.A. Davies. 1996. Application of focused ultrasound for the
1013 stimulation of neural structures. *Ultrasound Med Biol*. 22:179-192.
1014 Giese, K.P., J.F. Storm, D. Reuter, N.B. Fedorov, L.R. Shao, T. Leicher, O. Pongs, and A.J. Silva.
1015 1998. Reduced K+ channel inactivation, spike broadening, and after-hyperpolarization in
1016 Kvbeta1.1-deficient mice with impaired learning. *Learn Mem*. 5:257-273.
1017 Gonzalez, J.A., L.T. Jensen, S.E. Doyle, M. Miranda-Anaya, M. Menaker, L. Fugger, D.A. Bayliss,
1018 and D. Burdakov. 2009. Deletion of TASK1 and TASK3 channels disrupts intrinsic
1019 excitability but does not abolish glucose or pH responses of orexin/hypocretin neurons.
1020 *Eur J Neurosci*. 30:57-64.
1021 Gu, N., K. Vervaeke, and J.F. Storm. 2007. BK potassium channels facilitate high-frequency firing
1022 and cause early spike frequency adaptation in rat CA1 hippocampal pyramidal cells. *J*
1023 *Physiol*. 580:859-882.
1024 Hand, J.W. 1998. Ultrasound hyperthermia and the prediction of heating. *In* Ultrasound in
1025 Medicine. F. Duck, A. Baker and H. Starritt, editors. Institute of Physics Publishing,
1026 Philadelphia, PA.
1027 Harper, C.A. 2006. Handbook of plastics technologies: the complete guide to properties and
1028 performance. *In*. McGraw-Hill, New York, NY.
1029 Hille, B. 2001. Ion Channels of Excitable Membranes. 3rd
1030 .ed. Sinauer Associates, Inc., Sunderland, MA.
1031 Kanda, H., J. Ling, S. Tonomura, K. Noguchi, S. Matalon, and J.G. Gu. 2019. TREK-1 and TRAAK
1032 Are Principal K(+) Channels at the Nodes of Ranvier for Rapid Action Potential
1033 Conduction on Mammalian Myelinated Afferent Nerves. *Neuron*. 104:960-971 e967.
1034 Kang, D., C. Choe, and D. Kim. 2005. Thermosensitivity of the two-pore domain K+ channels
1035 TREK-2 and TRAAK. *J Physiol*. 564:103-116.

1036 Khaliq, Z.M., and B.P. Bean. 2010. Pacemaking in dopaminergic ventral tegmental area neurons:
1037 depolarizing drive from background and voltage-dependent sodium conductances. *J*
1038 *Neurosci*. 30:7401-7413.
1039 Kim, J., D.S. Wei, and D.A. Hoffman. 2005. Kv4 potassium channel subunits control action
1040 potential repolarization and frequency-dependent broadening in rat hippocampal CA1
1041 pyramidal neurones. *J Physiol*. 569:41-57.
1042 King, R.L., J.R. Brown, W.T. Newsome, and K.B. Pauly. 2013. Effective parameters for
1043 ultrasound-induced in vivo neurostimulation. *Ultrasound Med Biol*. 39:312-331.
1044 Kloda, A., L. Lua, R. Hall, D.J. Adams, and B. Martinac. 2007. Liposome reconstitution and
1045 modulation of recombinant N-methyl-D-aspartate receptor channels by membrane
1046 stretch. *Proc Natl Acad Sci U S A*. 104:1540-1545.
1047 Kole, M.H. 2011. First node of Ranvier facilitates high-frequency burst encoding. *Neuron*.
1048 71:671-682.
1049 Krasovitski, B., V. Frenkel, S. Shoham, and E. Kimmel. 2011. Intramembrane cavitation as a
1050 unifying mechanism for ultrasound-induced bioeffects. *Proc Natl Acad Sci U S A*.
1051 108:3258-3263.
1052 Kubanek, J., J. Shi, J. Marsh, D. Chen, C. Deng, and J. Cui. 2016. Ultrasound modulates ion
1053 channel currents. *Sci Rep*. 6:24170.
1054 Kwok, R., and E. Evans. 1981. Thermoelasticity of large lecithin bilayer vesicles. *Biophys J*.
1055 35:637-652.
1056 Laitko, U., and C.E. Morris. 2004. Membrane tension accelerates rate-limiting voltage-
1057 dependent activation and slow inactivation steps in a Shaker channel. *J Gen Physiol*.
1058 123:135-154.
1059 Lee, S.A., H.A.S. Kamimura, M.T. Burgess, and E.E. Konofagou. 2020. Displacement imaging for
1060 focused ultrasound peripheral nerve neuromodulation. *IEEE Trans Med Imaging*.
1061 Leighton, T.G. 1998. An introduction to acoustic cavitation. *In* Ultrasound in Medicine. F. Duck,
1062 A. Baker and H. Starritt, editors. Institute of Physics Publishing, Philadelphia, PA.
1063 Leterrier, C. 2018. The Axon Initial Segment: An Updated Viewpoint. *J Neurosci*. 38:2135-2145.
1064 Lien, C.C., and P. Jonas. 2003. Kv3 potassium conductance is necessary and kinetically optimized
1065 for high-frequency action potential generation in hippocampal interneurons. *J Neurosci*.
1066 23:2058-2068.
1067 Liu, P.W., and B.P. Bean. 2014. Kv2 channel regulation of action potential repolarization and
1068 firing patterns in superior cervical ganglion neurons and hippocampal CA1 pyramidal
1069 neurons. *J Neurosci*. 34:4991-5002.
1070 Lothet, E.H., K.M. Shaw, H. Lu, J. Zhuo, Y.T. Wang, S. Gu, D.B. Stolz, E.D. Jansen, C.C. Horn, H.J.
1071 Chiel, and M.W. Jenkins. 2017. Selective inhibition of small-diameter axons using
1072 infrared light. *Sci Rep*. 7:3275.
1073 MacKenzie, G., N.P. Franks, and S.G. Brickley. 2015. Two-pore domain potassium channels
1074 enable action potential generation in the absence of voltage-gated potassium channels.
1075 *Pflugers Arch*. 467:989-999.
1076 Madison, D.V., and R.A. Nicoll. 1984. Control of the repetitive discharge of rat CA 1 pyramidal
1077 neurones in vitro. *J Physiol*. 354:319-331.

1078 Maingret, F., I. Lauritzen, A.J. Patel, C. Heurteaux, R. Reyes, F. Lesage, M. Lazdunski, and E.
1079 Honore. 2000. TREK-1 is a heat-activated background K(+) channel. *EMBO J*. 19:2483-
1080 2491.
1081 Malinow, R., and R.W. Tsien. 1990. Presynaptic enhancement shown by whole-cell recordings
1082 of long-term potentiation in hippocampal slices. *Nature*. 346:177-180.
1083 Marinc, C., C. Derst, H. Pruss, and R.W. Veh. 2014. Immunocytochemical localization of TASK-3
1084 protein (K2P9.1) in the rat brain. *Cell Mol Neurobiol*. 34:61-70.
1085 Menz, M.D., O. Oralkan, P.T. Khuri-Yakub, and S.A. Baccus. 2013. Precise neural stimulation in
1086 the retina using focused ultrasound. *J Neurosci*. 33:4550-4560.
1087 Menz, M.D., P. Ye, K. Firouzi, A. Nikoozadeh, K.B. Pauly, P. Khuri-Yakub, and S.A. Baccus. 2019.
1088 Radiation Force as a Physical Mechanism for Ultrasonic Neurostimulation of the Ex Vivo
1089 Retina. *J Neurosci*. 39:6251-6264.
1090 Mihran, R.T., F.S. Barnes, and H. Wachtel. 1990. Temporally-specific modification of myelinated
1091 axon excitability in vitro following a single ultrasound pulse. *Ultrasound Med Biol*.
1092 16:297-309.
1093 Min, B.K., A. Bystritsky, K.I. Jung, K. Fischer, Y. Zhang, L.S. Maeng, S.I. Park, Y.A. Chung, F.A.
1094 Jolesz, and S.S. Yoo. 2011. Focused ultrasound-mediated suppression of chemically-
1095 induced acute epileptic EEG activity. *BMC Neurosci*. 12:23.
1096 Mizrahi, N., E.H. Zhou, G. Lenormand, R. Krishnan, D. Weihs, J.P. Butler, D.A. Weitz, J.J.
1097 Fredberg, and E. Kimmel. 2012. Low intensity ultrasound perturbs cytoskeleton
1098 dynamics. *Soft Matter*. 8:2438-2443.
1099 Morris, C.E., and P.F. Juranka. 2007. Nav channel mechanosensitivity: activation and
1100 inactivation accelerate reversibly with stretch. *Biophys J*. 93:822-833.
1101 Needham, D., and R.S. Nunn. 1990. Elastic deformation and failure of lipid bilayer membranes
1102 containing cholesterol. *Biophys J*. 58:997-1009.
1103 Oh, S.J., J.M. Lee, H.B. Kim, J. Lee, S. Han, J.Y. Bae, G.S. Hong, W. Koh, J. Kwon, E.S. Hwang, D.H.
1104 Woo, I. Youn, I.J. Cho, Y.C. Bae, S. Lee, J.W. Shim, J.H. Park, and C.J. Lee. 2020. Ultrasonic
1105 Neuromodulation via Astrocytic TRPA1. *Curr Biol*. 30:948.
1106 Owen, S.F., M.H. Liu, and A.C. Kreitzer. 2019. Thermal constraints on in vivo optogenetic
1107 manipulations. *Nat Neurosci*. 22:1061-1065.
1108 Pan, Z., T. Kao, Z. Horvath, J. Lemos, J.Y. Sul, S.D. Cranstoun, V. Bennett, S.S. Scherer, and E.C.
1109 Cooper. 2006. A common ankyrin-G-based mechanism retains KCNQ and NaV channels
1110 at electrically active domains of the axon. *J Neurosci*. 26:2599-2613.
1111 Paris, L., I. Marc, B. Charlot, M. Dumas, J. Valmier, and F. Bardin. 2017. Millisecond infrared
1112 laser pulses depolarize and elicit action potentials on in-vitro dorsal root ganglion
1113 neurons. *Biomed Opt Express*. 8:4568-4578.
1114 Plaksin, M., E. Kimmel, and S. Shoham. 2016. Cell-Type-Selective Effects of Intramembrane
1115 Cavitation as a Unifying Theoretical Framework for Ultrasonic Neuromodulation.
1116 *eNeuro*. 3.
1117 Prieto, M.L., K. Firouzi, B.T. Khuri-Yakub, and M. Maduke. 2018. Activation of Piezo1 but Not
1118 NaV1.2 Channels by Ultrasound at 43 MHz. *Ultrasound Med Biol*. 44:1217-1232.
1119 Prieto, M.L., O. Oralkan, B.T. Khuri-Yakub, and M.C. Maduke. 2013. Dynamic response of model
1120 lipid membranes to ultrasonic radiation force. *PLoS One*. 8:e77115.

1121 Qiu, Z., J. Guo, S. Kala, J. Zhu, Q. Xian, W. Qiu, G. Li, T. Zhu, L. Meng, R. Zhang, H.C. Chan, H.
1122 Zheng, and L. Sun. 2019. The Mechanosensitive Ion Channel Piezo1 Significantly
1123 Mediates In Vitro Ultrasonic Stimulation of Neurons. *iScience*. 21:448-457.
1124 Rashid, B., M. Destrade, and M.D. Gilchrist. 2012. Mechanical characterization of brain tissue in
1125 compression at dynamic strain rates. *J Mech Behav Biomed Mater*. 10:23-38.
1126 Rashid, B., M. Destrade, and M.D. Gilchrist. 2013. Mechanical characterization of brain tissue in
1127 simple shear at dynamic strain rates. *J Mech Behav Biomed Mater*. 28:71-85.
1128 Ricca, B.L., G. Venugopalan, and D.A. Fletcher. 2013. To pull or be pulled: parsing the multiple
1129 modes of mechanotransduction. *Curr Opin Cell Biol*. 25:558-564.
1130 Richter, C.P., A.I. Matic, J.D. Wells, E.D. Jansen, and J.T. Walsh, Jr. 2011. Neural stimulation with
1131 optical radiation. *Laser Photon Rev*. 5:68-80.
1132 Sarvazyan, A.P., O.V. Rudenko, and W.L. Nyborg. 2010. Biomedical applications of radiation
1133 force of ultrasound: historical roots and physical basis. *Ultrasound Med Biol*. 36:1379-
1134 1394.
1135 Schewe, M., E. Nematian-Ardestani, H. Sun, M. Musinszki, S. Cordeiro, G. Bucci, B.L. de Groot,
1136 S.J. Tucker, M. Rapedius, and T. Baukrowitz. 2016. A Non-canonical Voltage-Sensing
1137 Mechanism Controls Gating in K2P K(+) Channels. *Cell*. 164:937-949.
1138 Seeger, H.M., L. Aldrovandi, A. Alessandrini, and P. Facci. 2010. Changes in single K(+) channel
1139 behavior induced by a lipid phase transition. *Biophys J*. 99:3675-3683.
1140 Selfridge, A.R. 1985. Approximate Material Properties in Isotropic Materials. *Ieee T Son*
1141 *Ultrason*. 32:381-394.
1142 Shah, M.M., M. Migliore, I. Valencia, E.C. Cooper, and D.A. Brown. 2008. Functional significance
1143 of axonal Kv7 channels in hippocampal pyramidal neurons. *Proc Natl Acad Sci U S A*.
1144 105:7869-7874.
1145 Shao, L.R., R. Halvorsrud, L. Borg-Graham, and J.F. Storm. 1999. The role of BK-type Ca2+-
1146 dependent K+ channels in spike broadening during repetitive firing in rat hippocampal
1147 pyramidal cells. *J Physiol*. 521 Pt 1:135-146.
1148 Shapiro, M.G., K. Homma, S. Villarreal, C.P. Richter, and F. Bezanilla. 2012. Infrared light excites
1149 cells by changing their electrical capacitance. *Nat Commun*. 3:736.
1150 Tabarean, I.V., and C.E. Morris. 2002. Membrane stretch accelerates activation and slow
1151 inactivation in Shaker channels with S3-S4 linker deletions. *Biophys J*. 82:2982-2994.
1152 Talley, E.M., G. Solorzano, Q. Lei, D. Kim, and D.A. Bayliss. 2001. Cns distribution of members of
1153 the two-pore-domain (KCNK) potassium channel family. *J Neurosci*. 21:7491-7505.
1154 Taverna, S., T. Tkatch, A.E. Metz, and M. Martina. 2005. Differential expression of TASK
1155 channels between horizontal interneurons and pyramidal cells of rat hippocampus. *J*
1156 *Neurosci*. 25:9162-9170.
1157 Taylor, R.E. 1965. Impedance of the squid axon membrane. *J Cell Comp Physiol*. 66:21-25.
1158 Thijssen, J.M., H.J. Mol, and M.R. Timmer. 1985. Acoustic parameters of ocular tissues.
1159 *Ultrasound Med Biol*. 11:157-161.
1160 Tsui, P.H., S.H. Wang, and C.C. Huang. 2005. In vitro effects of ultrasound with different
1161 energies on the conduction properties of neural tissue. *Ultrasonics*. 43:560-565.
1162 Tufail, Y., A. Matyushov, N. Baldwin, M.L. Tauchmann, J. Georges, A. Yoshihiro, S.I. Tillery, and
1163 W.J. Tyler. 2010. Transcranial pulsed ultrasound stimulates intact brain circuits. *Neuron*.
1164 66:681-694.

1165 Tyler, W.J., S.W. Lani, and G.M. Hwang. 2018. Ultrasonic modulation of neural circuit activity.
1166 *Curr Opin Neurobiol*. 50:222-231.
1167 Tyler, W.J., Y. Tufail, M. Finsterwald, M.L. Tauchmann, E.J. Olson, and C. Majestic. 2008. Remote
1168 excitation of neuronal circuits using low-intensity, low-frequency ultrasound. *PLoS One*.
1169 3:e3511.
1170 Walsh, A.J., G.P. Tolstykh, S. Martens, B.L. Ibey, and H.T. Beier. 2016. Action potential block in
1171 neurons by infrared light. *Neurophotonics*. 3:040501.
1172 Wang, J., and O.P. Hamill. 2020. Piezo2, a pressure sensitive channel is expressed in select
1173 neurons of
1174 the mouse brain: a putative mechanism for synchronizing neural
1175 networks by transducing intracranial pressure pulses. *bioRxiv*.
1176 Wells, J., C. Kao, P. Konrad, T. Milner, J. Kim, A. Mahadevan-Jansen, and E.D. Jansen. 2007.
1177 Biophysical mechanisms of transient optical stimulation of peripheral nerve. *Biophys J*.
1178 93:2567-2580.
1179 White, S.H., and T.E. Thompson. 1973. Capacitance, area, and thickness variations in thin lipid
1180 films. *Biochim Biophys Acta*. 323:7-22.
1181 Wu, J., and W.L. Nyborg. 2008. Ultrasound, cavitation bubbles and their interaction with cells.
1182 *Adv Drug Deliv Rev*. 60:1103-1116.
1183 Yamada-Hanff, J., and B.P. Bean. 2015. Activation of Ih and TTX-sensitive sodium current at
1184 subthreshold voltages during CA1 pyramidal neuron firing. *J Neurophysiol*. 114:2376-
1185 2389.
1186 Ye, P.P., J.R. Brown, and K.B. Pauly. 2016. Frequency Dependence of Ultrasound
1187 Neurostimulation in the Mouse Brain. *Ultrasound Med Biol*. 42:1512-1530.
1188 Yoo, S., D.R. Mittelstein, R. Hurt, J. Lacroix, and M.G. Shapiro. 2020. Focused ultrasound excites
1189 neurons via mechanosensitive calcium accumulation and ion channel amplification.
1190 *bioRxiv*.
1191 Young, R.R., and E. Henneman. 1961. Functional effects of focused ultrasound on mammalian
1192 nerves. *Science*. 134:1521-1522.
1193 Yue, C., and Y. Yaari. 2004. KCNQ/M channels control spike afterdepolarization and burst
1194 generation in hippocampal neurons. *J Neurosci*. 24:4614-4624.
1195 Zachs, D.P., S.J. Offutt, R.S. Graham, Y. Kim, J. Mueller, J.L. Auger, N.J. Schuldt, C.R.W. Kaiser,
1196 A.P. Heiller, R. Dutta, H. Guo, J.K. Alford, B.A. Binstadt, and H.H. Lim. 2019. Noninvasive
1197 ultrasound stimulation of the spleen to treat inflammatory arthritis. *Nat Commun*.
1198 10:951.
1199 Zhou, D., S. Lambert, P.L. Malen, S. Carpenter, L.M. Boland, and V. Bennett. 1998. AnkyrinG is
1200 required for clustering of voltage-gated Na channels at axon initial segments and for
1201 normal action potential firing. *J Cell Biol*. 143:1295-1304.
1202 Zhu, X., J.W. Lin, and M.Y. Sander. 2019. Infrared inhibition and waveform modulation of action
1203 potentials in the crayfish motor axon. *Biomed Opt Express*. 10:6580-6594.
1204

1205

1206 **SUPPLEMENTAL MATERIALS**

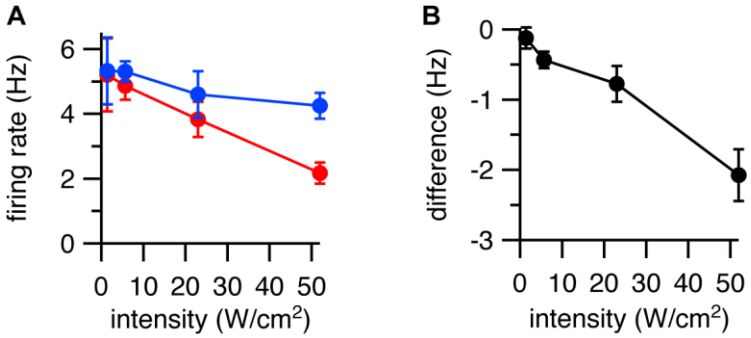

1207

1208 **Supplemental Figure 1. Effects of ultrasound at different intensities on firing rate. A.** Mean (±

1209 SEM) action potential firing rate with (*red*) or without (*blue*) a 1-s ultrasound pulse at various

1210 intensities starting 200 ms after the start of a 2-s current step, as measured during the period of

1211 overlap between the ultrasound and current stimuli, or during the same time period in the

1212 absence of ultrasound. N = 4 cells, except for 6 W/cm^2, where N = 3 cells. **B.** As in panel A, but

1213 showing the difference in firing rate between the ultrasound and control conditions.

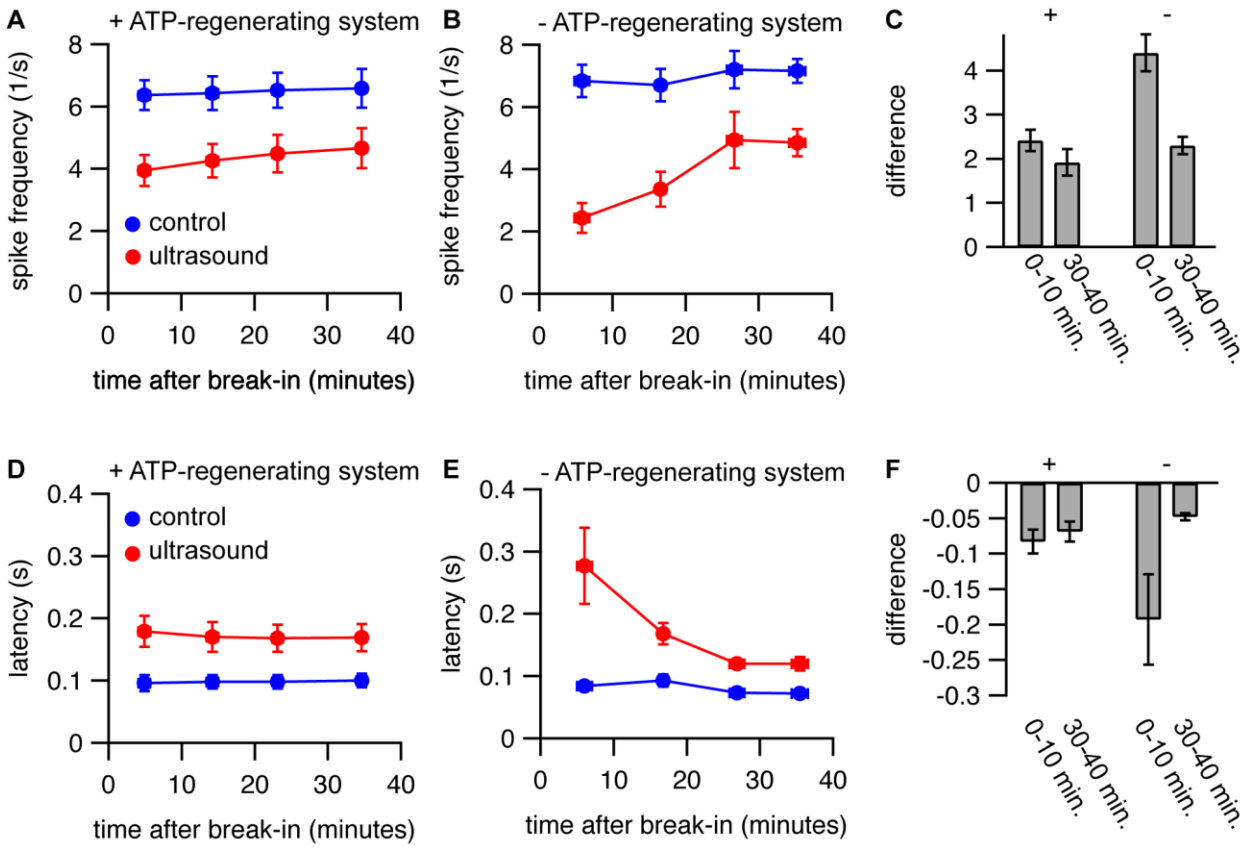

Supplemental Figure 2. An ATP-regenerating internal solution stabilizes the response to ultrasound. A-B. Mean (±SEM) spike rates during the first 500 ms of a current step in the presence (*red circles*) and absence (*blue circles*) of a 1-s ultrasound application starting 500 ms before the current step, as a function of time relative to break-in (establishment of whole-cell recording configuration). The internal solution contained 10 Na-phosphocreatine with (A) or without (B) 50 U/mL creatine phosphokinase to provide an ATP-regenerating system. Spike rates were measured at various time points between 0 and 10, 10 and 20, 20 and 30, and 30 and 40 minutes after break-in. The x-values represent the mean start time for the protocol to measure spike rates (which comprised 2 minutes of recording time) with horizontal error bars (in some cases smaller than the symbol size) representing the SEM. The amplitude of the current step was adjusted over time to maintain spiking behavior as close as possible to that at

1226 the start of the experiment. **C.** Mean (±SEM) difference in spike rate between the control and
1227 ultrasound conditions for measurements at 1-10 minutes after break-in and 30-40 minutes
1228 after break-in, with (*left*) or without (*right*) the ATP-regenerating system. The difference was
1229 only statistically significant without the ATP-regenerating system (P = 0.11, with; and P =
1230 0.0064, without). **D-F.** Same as A-B, but for latency to the first action potential following the
1231 start of the current step. N = 10 cells with and N = 6 cells without the ATP-regenerating system.
1232 The difference was not statistically significant for either group (P = 0.21, with; and P = 0.089,
1233 without).
1234

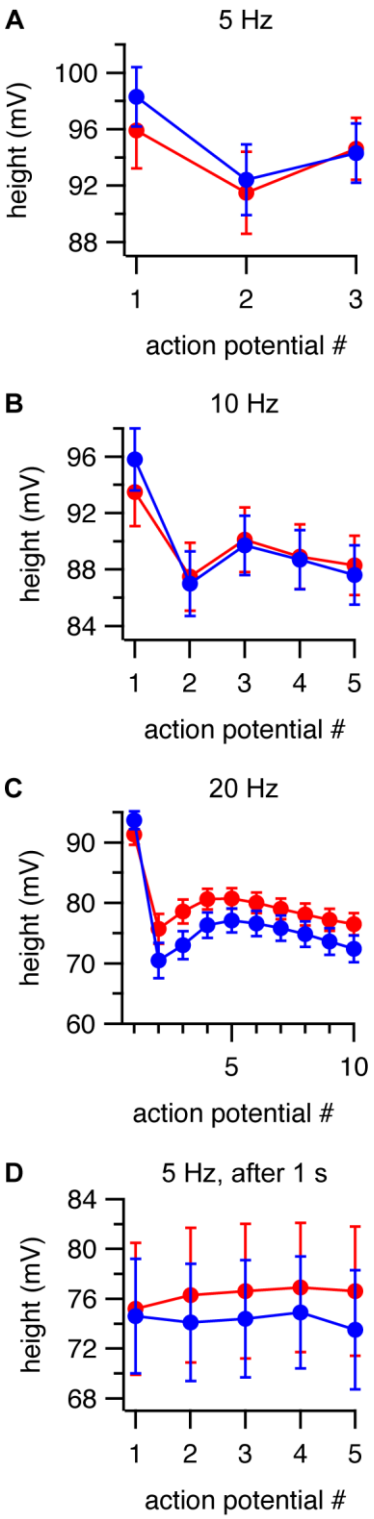

1235

1236 **Supplemental Figure 3. Effects of ultrasound on action potential height. A-C.** Mean (±SEM)

1237 action potential heights as a function of action potential number in the presence (*red*) and

absence (*blue*) of a 1-s ultrasound pulse starting 500 ms before the current step, for cells firing at an average firing rates (as measured during the first 500 ms of the current step) of approximately 5 Hz (N = 13), 10 Hz (N = 15), and 20 Hz (N = 13) in the control condition. **D.** As in A-C, but with ultrasound applied 1 s after the start of a 3-s current step, for cells firing at an average firing rate of approximately 5 Hz in the control condition, with firing rate determined in a 1-s window starting 1 s after the current step (corresponding to the time period of the ultrasound stimulus), and action potential number relative to the start of the ultrasound stimulus (N = 6). Note that the y-axes do not begin at zero.

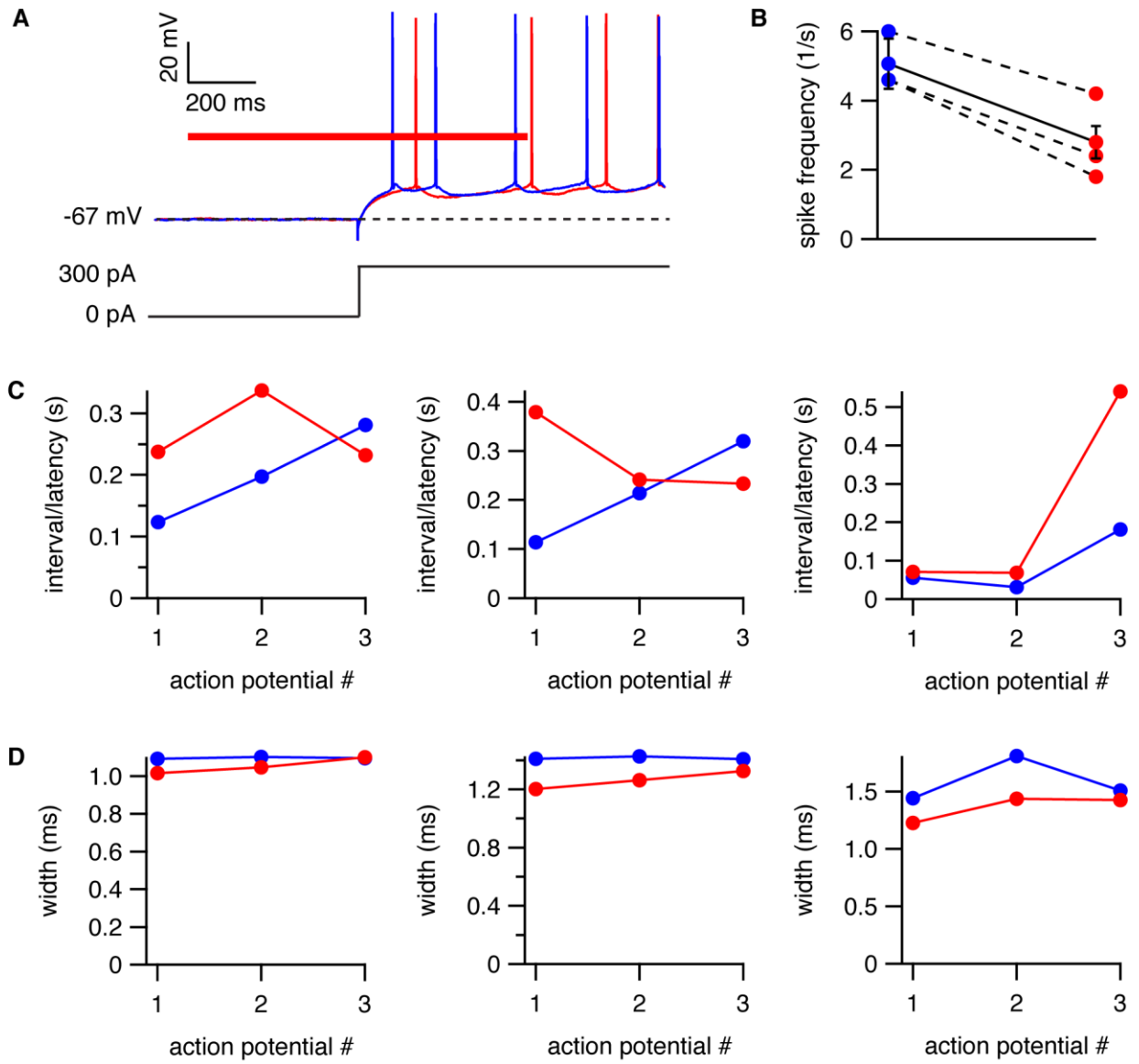

1247

1248 **Supplemental Figure 4. Effects of ultrasound on action potential firing and waveform at near-**
1249 **physiological temperature. A.** Example voltage traces showing inhibition of action potential
1250 firing by ultrasound at 30°C. The response to a 300-pA current step is shown with (*red voltage*
1251 *trace*) and without (*blue voltage trace*) a 1-s ultrasound pulse (*red bar*) applied 500 ms before
1252 the start of the current step. The *dashed line* indicates the resting membrane voltage. **B.** Mean
1253 (± SEM, N =3) spike frequency during the first 500 ms of the current step (corresponding to the
1254 period of overlap between the current and ultrasound stimuli, or the equivalent time period in
1255 the absence of ultrasound) for the protocol shown in panel A for the control (*blue*) and
1256 ultrasound (*red*) conditions, for cells firing at an average spike frequency of approximately 5 Hz
1257 in the absence of ultrasound. Data points for the individual cells are shown connected by
1258 *dashed lines*. (Compare Figure 1E.) **C.** Latency between the start of the current step and the first
1259 action potential, and between the first and second, and second and third action potentials, for
1260 the control (*blue*) and ultrasound (*red*) conditions for three individual cells. (Compare Figure

1261 4A.) **D.** As in panel C, but for effects of ultrasound on action potential width. (Compare Figure
1262 6A.)